Holocene faulting in the Bellingham forearc basin: Upper-plate deformation at the northern end of the Cascadia subduction zone

Harvey M. Kelsey,[1] Brian L. Sherrod,[2] Richard J. Blakely,[3] and Ralph A. Haugerud[2]

[1]   The northern Cascadia forearc takes up most of the strain transmitted northward via the Oregon Coast block from the northward-migrating Sierra Nevada block. The north-south contractional strain in the forearc manifests in upper-plate faults active during the Holocene, the northern-most components of which are faults within the Bellingham Basin. The Bellingham Basin is the northern of four basins of the actively deforming northern Cascadia forearc. A set of Holocene faults, Drayton Harbor, Birch Bay, and Sandy Point faults, occur within the Bellingham Basin and can be traced from onshore to offshore using a combination of aeromagnetic lineaments, paleoseismic investigations and scarps identified using LiDAR imagery. With the recognition of such Holocene faults, the northernmost margin of the actively deforming Cascadia forearc extends 60 km north of the previously recognized limit of Holocene forearc deformation. Although to date no Holocene faults are recognized at the northern boundary of the Bellingham Basin, which is 15 km north of the international border, there is no compelling tectonic reason to expect that Holocene faults are limited to south of the international border.

1. Introduction

[2]   Actively deforming forearcs are characteristic of many subduction zone plate boundaries and exhibit seismic hazards from both megathrust and upper-plate earthquakes. Substantial plate boundary deformation is accommodated in the forearc. Examples of emergent, actively deforming forearcs include those at the Hikurangi subduction zone, which is partially exposed along the east coast of North Island, New Zealand [*Hull*, 1990; *Cashman et al.*, 1992; *Berryman*, 1993; *Kelsey et al.*, 1995, 1998; *Little et al.*, 2009] and the partially emergent Nankai forearc in Japan that hosted the 1995 Kobe, Japan, earthquake [*Kanamori*, 1995; *Pollitz and Sacks*, 1997]. Emergent forearcs are home to many of Earth's large population centers. A case in point is the northern Cascadia forearc in northwest Washington and southwest British Columbia (Figure 1b).

[3]   The Cascadia forearc is caught between a northward migrating Sierra Nevada block and a stationary Canadian buttress [*Wells et al.*, 1998; *McCaffrey et al.*, 2000, 2007] (Figure 1). The resulting north-south strain is not distributed uniformly throughout the Cascadia forearc, however, but rather is accommodated mostly by a system of crustal faults and folds in the northernmost part of the forearc between Olympia and the Canadian border (Figure 1). Most of these faults produced M6 or greater earthquakes in Holocene time, and some of them are tied to the structural evolution of four major basins beneath the Puget lowland: the Tacoma, Seattle, Everett, and Bellingham basins. We refer to this region of active deformation as the northern Cascadia forearc.

[4]   Despite the above conceptual model for the northern Cascadia forearc, which is well grounded in GPS geodetic measurements and paleoseismic investigations of Holocene faults, the structures that must necessarily accommodate forearc strain are incompletely understood. In particular, the hypothesis of a collective northward migration of the Sierra Nevada, Oregon Coast and deforming Cascadia forearc blocks implies that the northern, leading edge of the northern Cascadia forearc may be a dynamic boundary zone that incorporates new active deformation.

[5]   What is the northern end of the northern Cascadia forearc and where are the active faults that comprise this northern boundary? *Wells et al.* [1998] proposed that the northern Cascadia forearc impinged northward against stable North America with a geodetically determined stable buttress in southern British Columbia (Figure 1a). The model of *Wells et al.* [1998] focused on Quaternary faults in the southern Puget lowland but did not suggest a northern limit of forearc deformation. Subsequent tectonic summaries [*Johnson et al.*, 2001, 2004b] adopted this model and noted that the northernmost evidence of Quaternary deformation within the Cascadia forearc was at the latitude of the Devils Mountain fault zone (Figure 1b). But recent investigations

---

[1]Department of Geology, Humboldt State University, Arcata, California, USA.
[2]U.S. Geological Survey, University of Washington, Seattle, Washington, USA.
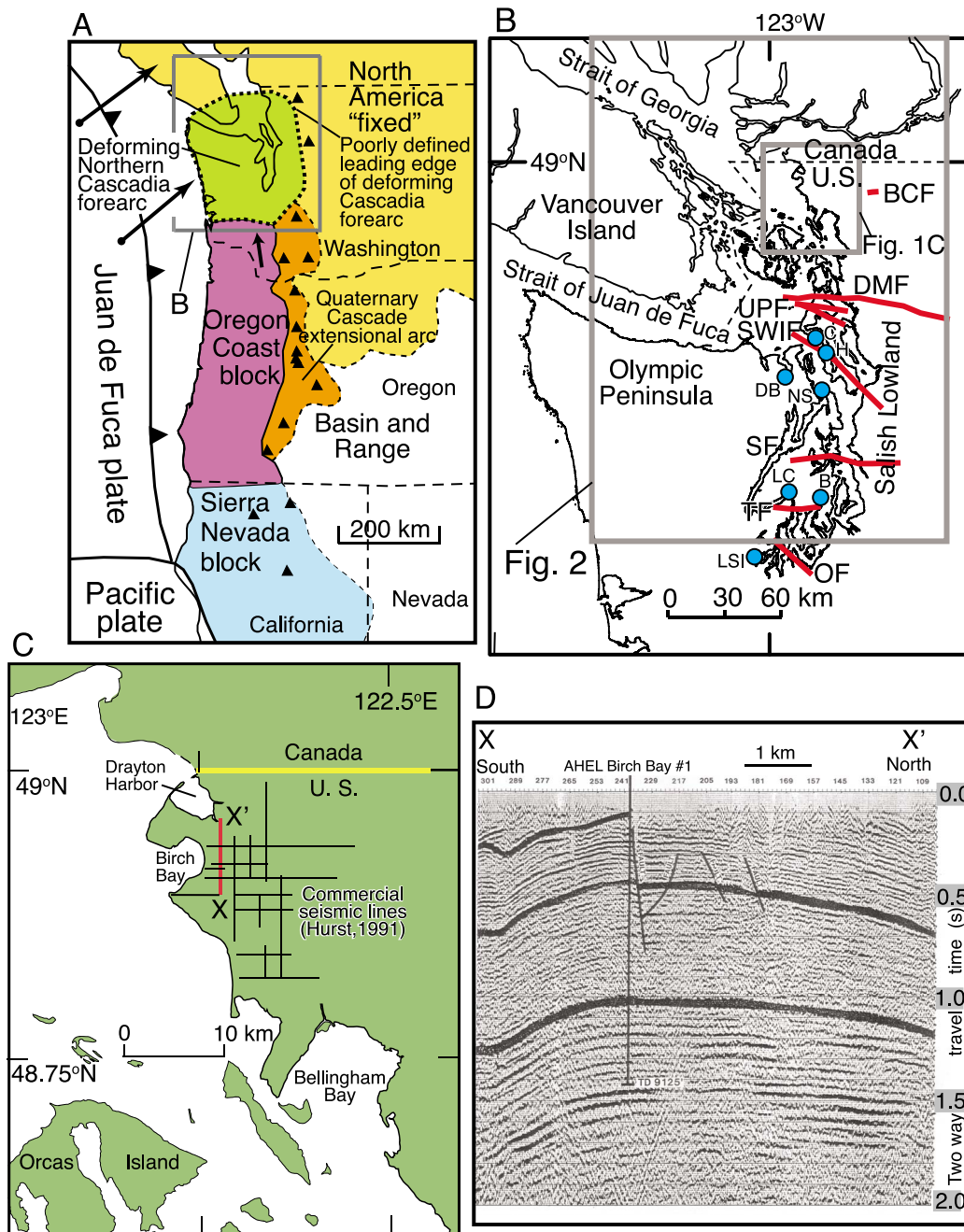[3]U.S. Geological Survey, Menlo Park, California, USA.

Figure 1. (a) Tectonic map modified from *Wells at al.* [1998] showing Oregon coast block impinging northward on the deforming Cascadia forearc. Black triangles denote major volcanoes. Arrows at Cascadia deformation front show motion of Juan de Fuca plate relative to North America [after *McCaffrey et al.*, 2007]. (b) Northern Cascadia forearc showing known faults, mostly in southern and central Puget lowland, that accommodate Holocene north-south shortening. OF, Olympia fault; TF, Tacoma fault; SF, Seattle fault; SWIF, Southern Whidbey Island fault; UPF, Utsalady Point fault; DMF, Devils Mountain fault; BCF, Boulder Creek fault. Blue dots are sample sites (samples are uppermost 5 mm) for modern database diatom samples (n = number of stations): C, Crocket Lake, n = 19; H, Hancock Lake, n = 14; DB, Discovery Bay, n = 38; LC, Lynch Cove, n = 26; LSI, Little Skookum Inlet, n = 6; NS, North Spit, n = 4; and B, Burley, n = 3. (c) Northwesternmost Washington and southern British Columbia showing coastal study area from Canadian-U. S. border south to Bellingham Bay and showing location of seismic line depicted Figure 1d. (d) Reproduction of an approximately 6 km-long, north-trending seismic reflection profile 1.3 km east of Birch Bay, Washington [*Hurst*, 1991] showing Birch Bay anticline. This on-land seismic reflection line was one of many shot by American Hunter Exploration, Limited, near Birch Bay (track lines on Figure 1c). With the exception of *Hurst* [1991], the data are no longer available. The annotation on the seismic line is from the original publication and not pertinent to our discussion (see text).
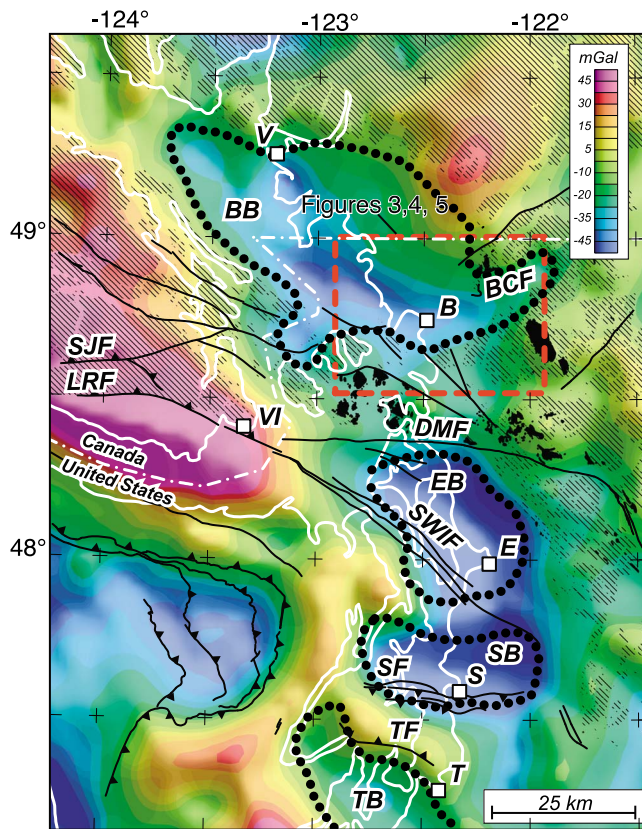
Figure 2. Isostatic residual gravity anomalies of the northern Cascadia forearc. Gravity data from Decade of North American Geology Bouguer gravity compilation, converted to isostatic residual anomalies using the method of *Simpson et al.* [1986]. Black lines are selected faults. Stipple pattern indicates pre-Tertiary exposures; black areas are pre-Tertiary ultramafic rocks, including Jurassic Fidalgo Complex. Black dotted lines outline gravity lows caused by sediment-filled basins. Cities: V, Vancouver; VI, Victoria; B, Bellingham; E, Everett; S, Seattle; T, Tacoma. Faults: BCF, Boulder Creek fault; SJF, San Juan fault; LRF, Leech River fault; DMF, Devils Mt. fault; SWIF, Southern Whidbey Island fault; SF, Seattle fault; TF, Tacoma fault. Basins: BB, Bellingham basin; EB, Everett basin; SB, Seattle basin; TB, Tacoma basin. Red dashed rectangle is area of Figures 3, 4, and 5.

[*Barnett et al.*, 2006] show that active faults, which accommodate north-south shortening, occur 60 km north of the predicted backstop of the Devils Mountain fault zone.

[6] The objective of this paper is to lay out a revised tectonic framework for the northern Cascadia forearc. We identify a tectonically active basin (Bellingham Basin) at the northern end of the forearc and describe Holocene faults that occur within this basin. These faults comprise part of the northern, leading edge of the deforming northern Cascadia forearc.

2. Geologic Setting

[7] Geodetic measurements confirm that the Cascadia forearc is moving northward to northwestward (North

America fixed reference frame) in response to margin-parallel migration of the Oregon Coast block [*McCaffrey et al.*, 2000; *Mazzotti et al.*, 2003]. The Cascadia forearc abuts against a rigid backstop to the north, causing the forearc to shorten at a rate of approximately 4.5 mm/yr [*Mazzotti et al.*, 2002; *McCaffrey et al.*, 2007]. This margin-parallel shortening is concentrated in the region of high crustal seismicity along the Puget lowland corridor between Olympia and the U. S.-Canadian border [*Mazzotti et al.*, 2002; *Hyndman et al.*, 2003], the region that we refer to as the northern Cascadia forearc.

[8] Numerous east-west or southeast-northwest trending, Holocene fault zones in the Puget lowland collectively accommodate north-south forearc shortening in the upper plate of the Cascadia subduction zone. These include, from south to north, the Olympia [*Sherrod*, 2001], Tacoma [*Sherrod et al.*, 2004], Seattle [*Bucknam et al.*, 1992; *Sherrod et al.*, 2000; *Blakely et al.*, 2002; *Nelson et al.*, 2003; *Brocher et al.*, 2004; *Kelsey et al.*, 2008], Southern Whidbey Island [*Johnson et al.*, 1996; *Kelsey et al.*, 2004; *Sherrod et al.*, 2005], Utsalady Point [*Johnson et al.*, 2004a], and Devils Mountain fault zones [*Johnson et al.*, 2001]. In addition, the Kendall trace of the Boulder Creek fault [*Haugerud et al.*, 2005; *Barnett et al.*, 2006] (Figure 1b) is a recently identified Holocene fault at the northern end of the contracting forearc.

[9] We adopt the term Bellingham Basin to identify the northern of four forearc basins of the northern Cascadia forearc (Figure 2). *Miller and Misch*'s [1963] *senso stricto* description of the Bellingham Basin placed basin inception in the mid Tertiary with the deposition of the Huntington Formation. Our geologic mapping (RJH) raises the question whether the Huntington Formation is indeed deposited on a structural unconformity; nonetheless the term Bellingham Basin aptly describes the structural basin, situated in northwest Washington and southern British Columbia, which has existed since the mid Tertiary. The eastern extent of the Bellingham Basin can be considered the same as the eastern extent of the broadly defined, modern physiographic Georgia Basin [*Gallup*, 1957], which lies between the Vancouver Island Coast Range and the Coast Ranges of southwestern British Columbia.

3. Research Approach

[10] Multiple investigative techniques enable us to characterize Holocene deformation within the Bellingham forearc basin and provide a context for interpreting the deformation at the northern end of the Cascadia forearc. We employ residual gravity data to define the Bellingham Basin as younger, lower density rocks that have accumulated in the basin. We then introduce aeromagnetic data to infer near-surface lithologic contacts, using gravity data to help constrain our interpretations. Using these potential-field data and LiDAR imagery, we investigate candidates for active faults and folds. Specifically, we use LiDAR data and field reconnaissance to identify likely field targets for subsequent paleoseismic investigation of faults, and then we use potential field data to reveal possible causative structures. At coastal paleoseismic sites, we assess abrupt changes in relative sea level to ascertain timing and magnitude of fault displacements. Where possible, ground- and boat-magnetic

surveys follow up at the locations of candidate active faults. Aeromagnetic, ground-magnetic, and boat-magnetic surveys aid in mapping the active traces of hypothesized faults farther onshore and offshore.

4. Geophysical and Structural Characteristics of the Bellingham Basin

4.1. The Bellingham Structural Basin

[11] A north-trending alignment of negative gravity anomalies along the Salish Lowland (Figure 1b) in western Oregon, Washington, and British Columbia reflects structural basins of the Cascadia forearc. These basins, extending from the Willamette Valley in Oregon to the Strait of Georgia in British Columbia, have diverse and complex tectonic origins, all ultimately caused by subduction of the Juan de Fuca plate beneath North America. Four basins in the Puget lowland are particularly well displayed in gravity anomalies: the Tacoma, Seattle, Everett, and Bellingham basins (Figure 2). The southern three of these basins (Tacoma, Seattle, and Everett) are in part structurally tied to crustal faults that cross the Puget lowland and have produced M_W 6.5–7.5 earthquakes in the last 15 ka. The Seattle fault, which produced a M_W 7 earthquake about 1100 years ago [*Bucknam et al.*, 1992], is an east-striking, north-verging thrust fault that has lifted its hanging wall (the Seattle uplift) up and over regions to the north, producing the Seattle basin now filled with up to 10 km of Oligocene and younger sedimentary rocks [e.g., *Johnson et al.*, 1994; *Pratt et al.*, 1997; *Brocher et al.*, 2001]. The basin began as "a discrete geologic element" at 40 Ma [*Johnson et al.*, 1994], and initiation of thrusting on the presently active strand of the Seattle fault occurred about 10 Ma with deformation of the Miocene Blakely Harbor Formation [*Johnson et al.*, 1999]. The active Tacoma fault lies along the southern margin of the Seattle uplift and forms the structural contact with the Tacoma basin to the south [*Johnson et al.*, 2004b; *Pratt et al.*, 1997]. The Everett basin is bounded on its north margin by the Devils Mountain fault [*Johnson et al.*, 2001] and is bounded in part along its southwest margin by the Southern Whidbey Island fault [*Johnson et al.*, 1996; *Kelsey et al.*, 2004; *Sherrod et al.*, 2008]. These large faults and basins evolved, at least in part, due to compressive forces established by the northward migration and clockwise rotation of the Washington forearc against stable regions to the north, a process that has continued at approximately steady rates for the last 10 to 15 Ma [e.g., *Wells et al.*, 1998; *McCaffrey et al.*, 2007].

[12] The prevailing published perspective is that the Devils Mountain fault (Figures 1 and 2) serves as the buttress between the northward migrating forearc and stable North America [e.g., *Johnson et al.*, 2001]. This hypothesis is inconsistent with the position of the Bellingham Basin, however, which lies well north of the Devils Mountain fault. The location of the Bellingham basin suggests either that the buttress lies somewhere north of the Bellingham basin or that the Bellingham Basin evolved independently of processes that formed the other Puget lowland basins. Recent paleoseismic studies of the Boulder Creek fault [*Barnett et al.*, 2006] (Figures 1 and 2) favor the former explanation. The Boulder Creek fault, which lies well north of the Devils Mountain fault near the Canadian border, and at the

northeast margin of the Bellingham Basin, has produced Holocene earthquakes and is apparently contributing to northward shortening of the forearc.

[13] An industry seismic line provides another line of evidence that the Bellingham Basin has experienced Quaternary northward shortening. Although data from an extensive on-land seismic survey northwest of Bellingham (track lines on Figure 1c) are no longer available, a small segment of one of the lines (X-X′, Figure 1c) was published two decades ago [*Hurst*, 1991] (Figure 1d). The 6-km long, north-trending seismic line is only available as an annotated figure from *Hurst* [1991], and the annotation highlights inferred small-displacement faults at the crest of an anticline. The anticline, with an approximate east-trending axis, is expressed in strata as young as the highest seismic reflections (Figure 1d). The highest seismic reflections represent horizons only tens to hundreds of meters below ground underlain by late Quaternary deposits [*Easterbrook*, 1976]. A reasonable inference, therefore, is that the anticline has grown during the Quaternary.

4.2. Concealed Crustal Structure Interpreted From Magnetic Anomalies

[14] The northern margin of the Bellingham basin, as defined by maximum gradients of the gravity anomaly and by bounding outcrops of pre-Tertiary rocks, trends southeast subparallel to, but 10–15 km north of, the U. S.-Canadian border. The emergent portion of the basin broadly defines the lowland between Bellingham and Vancouver, British Columbia. Our paleoseismic studies, described below, find evidence for late Holocene tectonic deformation in the Birch Bay-Drayton Harbor coastal zone within the Bellingham Basin. No faults or folds are mapped in the immediate area of Birch Bay, but such structures could be concealed by Pleistocene and younger glacial deposits that cover the Birch Bay area [*Easterbrook*, 1963, 1976]. Elsewhere in the Puget lowland, analysis of high-resolution aeromagnetic data has proven useful in mapping and characterizing active faults, where, in concert with LiDAR topographic surveys and follow-on trench excavations, a rich history of Holocene deformation is now being revealed [e.g., *Sherrod et al.*, 2008; *Blakely et al.*, 2002, 2009]. Here we investigate aeromagnetic data from the Bellingham area to explore for and map concealed faults that may be responsible for late Holocene deformation in the Bellingham Basin. We focus on the coastal area between Bellingham Bay and Drayton Harbor (Figure 1c).

[15] Magnetic data for northwesternmost Washington (Figure 3) were acquired in 1997 as part of an airborne magnetic survey of the entire Puget lowland [*Blakely et al.*, 1999]. Measurements were made at a nominal elevation of 250 m above terrain along north-south lines spaced 400 m apart. In our study area, measurement altitudes ranged between 230 and 260 m throughout the coastal lowland area, but were significantly higher over mountainous regions to the east. Total-field measurements were converted to anomaly values by subtraction of the International Geomagnetic Reference Field, updated to the date of the survey. The anomalies in Figure 3 are transformed to the north magnetic pole in order to reduce anomaly skewness and horizontal displacement caused by non-vertical directions of magnetization and ambient field [*Blakely*, 1995].
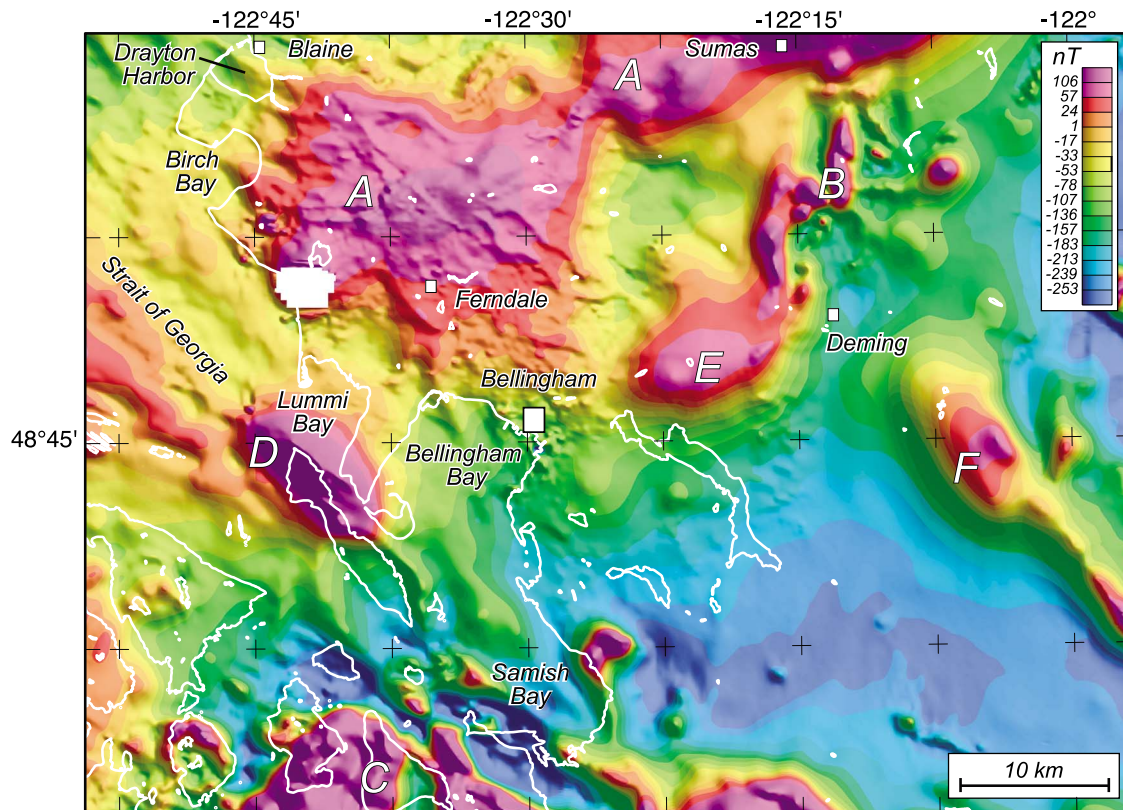
Figure 3. Magnetic anomalies of the Birch Bay study area. Color contours represent total-field magnetic anomaly values measured nominally 250 m above terrain over flat areas but significantly higher over mountainous regions [*Blakely et al.*, 1999]. Magnetic anomalies reduced to pole. White lines are coastlines and lakes. Letters indicate specific anomalies discussed in text. The white area on the coast between Birch Bay and Lummi Bay is located directly over an aluminum smelter operating at the time of the survey; the intense anomaly produced by the smelter was removed from the data prior to analysis.

4.2.1. Magnetic Lithologies in the Birch Bay Area

[16] The magnetic field of the Birch Bay study area (Figure 3) is characterized by numerous high-amplitude magnetic anomalies, most of which are not obviously associated with mapped geology. A broad positive anomaly extends southwestward from north of Vedder Mountain to the Strait of Georgia (Figure 3, label A), an area entirely covered by Pleistocene and younger glacial outwash and other young deposits. Glacial deposits in the Bellingham Basin lowland are weakly magnetic, with magnetic susceptibilities on the order of 3.0 SIU (Tables 1 and 2), consistent with measurements of glacial deposits elsewhere in the Puget lowland [*Sherrod et al.*, 2008]. While glacial deposits do produce low-amplitude anomalies in the Bellingham Basin lowland, they are insufficiently magnetic to produce the broad aspects of anomaly A. Thus, the lithologic source of anomaly A must lie concealed beneath the glacial deposits and within pre-Pleistocene basement.

[17] Most basement rocks exposed elsewhere in the study area are insufficiently magnetic to cause anomaly A. Tertiary exposures are mainly continental sedimentary rocks of the Chuckanut Formation [e.g., *Johnson*, 1982], with magnetic susceptibilities typically <1.0 SIU (Tables 1 and 2). Moreover, most pre-Tertiary rocks, where exposed in the area, are not obviously associated with large magnetic anomalies. There is one important exception, however; several high-

amplitude anomalies of the study area overlie pre-Tertiary ultramafic rocks, including anomalies over exposures north of the Boulder Creek fault (Figure 3, label B) and in parts of the San Juan Islands (Figure 3, label C). Ultramafic rocks can be strongly magnetic, especially when they contain serpentinite (Tables 1 and 2). By inference, concealed pre-Tertiary ultramafic rocks may be responsible for anomaly A and for other high-amplitude anomalies in the area, including anomalies over the northern part of Lummi Island (Figure 3, label D), immediately north of Whatcom Lake (Figure 3, label E), and northwest of the Twin Sisters Range (Figure 3, label F).

[18] We also consider the possibility that anomaly A and other anomalies in the study area are caused by lithologies unexposed in the study area. Well logs in the Bellingham area, for example, describe 100 to 200 m of Quaternary deposits overlying Miocene and older continental sediments that include a pebble conglomerate [*Hopkins*, 1968]. This Miocene conglomerate is not exposed in the study area, but well logs describe it as being similar to the Miocene Blakely Harbor Formation exposed elsewhere in the Puget lowland [*Fulmer*, 1975]. The Blakely Harbor Formation is significantly magnetic where it crops out on Bainbridge Island, and it produces pronounced linear magnetic anomalies where deformed by the Seattle fault [*Blakely et al.*, 2002]. It is possible that the concealed Miocene conglomerate

Table 1. Magnetic Susceptibility Measurements From the Bellingham Area[a]

Site	Longitude	Latitude	N	Average Magnetic Susceptibility SIU[b]	Standard Deviation SIU[b]	Site Description
1	−122.10493	48.89286	10	0.66	0.36	Eocene Chuckanut Formation (sandstone)
2	−122.08320	48.89091	10	0.45	0.03	Eocene Chuckanut Formation (siltstone)
3	−122.05042	48.88617	10	0.26	0.03	Eocene Chuckanut Formation (sandstone)
4	−122.04807	48.89040	10	0.10	0.02	Eocene Chuckanut Formation (arkosic sandstone)
5	−122.04736	48.89472	10	0.26	0.05	Eocene Chuckanut Formation (various lithologies)
6	−122.11102	48.89598	10	2.45	0.64	Pleistocene glacial outwash
7	−122.19313	48.95596	10	0.37	0.16	Pre-Tertiary metamorphic rock, highly altered
8	−122.20062	48.93760	10	3.09	2.68	Pleistocene conglomerate (ultramafic pebbles)
9	−122.20247	48.93795	10	4.60	4.88	Pre-Tertiary ultramafic
10	−122.21074	48.93502	10	11.77	8.05	Pre-Tertiary ultramafic
11	−122.00025	49.00025	10	5.01	2.00	Pleistocene glacial outwash (sand, diamict)
12	−122.66890	48.97890	10	2.43	0.55	Pleistocene glacial outwash, glacial marine drift
13	−122.66025	48.98820	10	2.22	0.98	Pleistocene gravel (large pebbles in sand)
14	−122.63509	48.97134	10	3.84	1.20	Pleistocene outwash (clay, medium sand)
15	−122.79494	48.97592	10	3.99	0.56	Pleistocene glacial marine drift (silt, fine sand)
16	−122.77715	48.89853	10	2.65	0.54	Pleistocene glacial marine drift
17	−122.48196	48.66859	10	0.94	0.84	Eocene Chuckanut Formation (sandstone)
18	−122.48248	48.67151	10	0.86	0.83	Eocene Chuckanut Formation (sandstone)
19	−122.49046	48.65152	10	1.15	0.30	Eocene Chuckanut Formation (sandstone)
20	−122.48995	48.70067	10	0.15	0.04	Eocene Chuckanut Formation

[a]Measurements made on in situ rocks using a Kappameter model KT-5.

[b]Average magnetic susceptibility and standard deviation expressed in SI units times 1000. Susceptibility is a dimensionless quantity, with a value that depends on the system of units. SIU is an abbreviation for *le Système international d'unités*, or International System of Units. Average values are geometric average of N samples.

encountered in wells is the cause of anomaly A, although ultramafic rocks are at least as likely a cause of anomaly A.

4.2.2. Magnetic Lineaments and Paleoseismic Deformation

[19] A complex pattern of short-wavelength, low-amplitude magnetic anomalies is superimposed on anomaly A in Figure 3 and may have implications for late-Holocene deformation observed at our paleoseismic sites. The short wavelengths of these anomalies indicate that they originate from near the topographic surface, within or just below Pleistocene glacial cover and above the source of the broader aspects of anomaly A itself. Figure 4 shows an attempt to illuminate these shallow-source magnetic anomalies. The procedure has two steps: original measurements were analytically continued to a surface 50 m higher than the elevation of the measurements and then subtracted from the original data. The procedure is equivalent to a discrete vertical derivative, a method that amplifies shallow-source anomalies at the expense of anomalies of deeper origin [*Blakely*, 1995]. Implementing this procedure, anomaly A has been subdued relative to lineaments originating from sources nearer the topographic surface (Figure 4).

[20] A large number of magnetic lineaments are evident in the filtered magnetic data (Figure 4), especially in the region east of Birch Bay and Drayton Harbor. Lineaments are typically less than 5 km in length, but in some cases extend for distances >10 km. Magnetic lineaments have a variety of possible explanations in this area. They may reflect, for example, shallow faults or folds in weakly magnetic Quaternary deposits, magnetic minerals concentrated by fluvial or sub-glacial processes, or concealed erosional unconformities. The magnetic lineaments in Figure 4 are similar in character to anomalies observed along the mainland portion of the Southern Whidbey Island fault south of Everett, where the lineaments are associated with LiDAR scarps and caused by offsets in late Pleistocene and younger glacial deposits [*Sherrod et al.*, 2008]. We consider the possibility that some of the lineaments in the Birch Bay area are similarly caused by shallow crustal faults.

[21] To assist with our interpretation, we applied a method that numerically and objectively calculates the position of contrasting magnetization from the shape of magnetic anomalies (Figure 4, black dots and black lines composed of black dots) [*Blakely*, 1995; *Phillips et al.*, 2007]. We use the term "magnetic contact" to specify contacts determined directly from anomaly amplitudes (rainbow colors) and magnetization contrasts (black dots) of Figure 4.

Table 2. Summary of Magnetic Susceptibility Measurements From the Bellingham Area

Lithology	Number of Sites	Number of Samples[a]	Average Magnetic Susceptibility[b]	Standard Deviation[b]	Confidence Interval[b,c]
Eocene Chuckanut Formation	9	90	0.54	0.38	0.06
Pleistocene glacial deposits	8	80	3.21	0.98	0.11
Pre-Tertiary ultramafic rocks	2	20	8.19	5.07	1.88

[a]Number of samples is the total number of measurements for each lithology.

[b]Average magnetic susceptibility, standard deviation and confidence interval all are expressed in SI units times 1000; see Table 1 for additional information.

[c]Confidence intervals are standard deviations divided by square root of the number of samples minus 1.
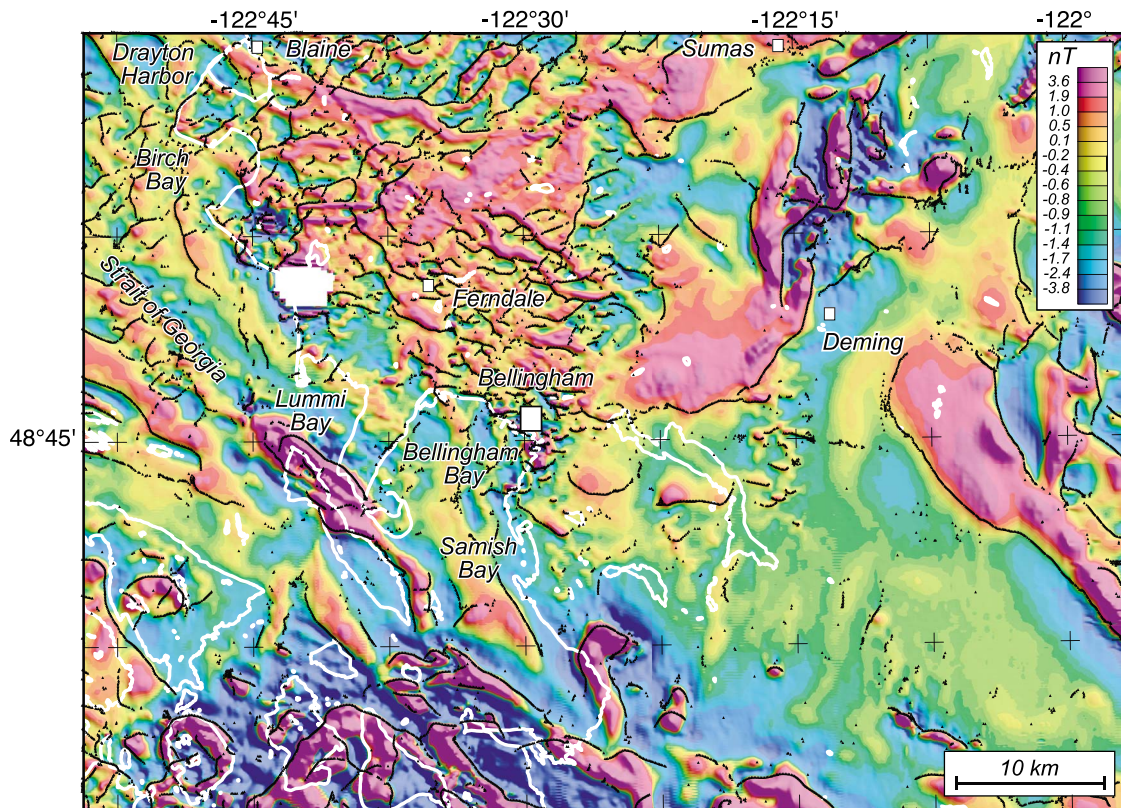
Figure 4. Magnetic anomalies of the Birch Bay study area filtered in order to emphasize shallow magnetic sources. Data from Figure 3 were continued upward 50 m, then subtracted from the original data. Black lines and dots indicate magnetic contacts calculated directly from magnetic data and discussed in text.

[22] A regional interpretation of gravity and magnetic anomalies (Figure 5), based on Figures 2, 3 and 4, delineates the most significant magnetic contacts as red-dotted lines, with hachures indicating the positive portion of the magnetic gradient. As noted above, the magnetic contacts identified in Figure 5 have a variety of possible geologic explanations. Considering that they lie within the forearc of the Cascadia subduction zone and in a region of modern north-south compression and active faulting, we believe it is prudent to consider the possibility that some of the lineaments represent Holocene deformation. Several northwest-striking magnetic contacts are evident crossing from offshore to onshore regions in the vicinity of Birch Bay, Lummi Bay and Drayton Harbor. Each of these magnetic contacts is spatially associated with sites of inferred late-Holocene deformation, as discussed below, suggesting that these magnetic contacts could be caused by concealed active faults.

4.2.2.1. Birch Bay Magnetic Contact

[23] A northwest-striking magnetic contact passes through Birch Bay (Figure 5, label BB) and makes landfall at the south end of our Birch Bay paleoseismic site (discussed below). At this site, a late Holocene beach platform to the north of the magnetic contact is elevated ~4 m relative to the modern beach platform, but this elevated platform is absent to the south. The sense of the magnetic anomaly, with higher anomaly values north of the magnetic contact, is consistent with a north-side-up fault located at the point of inflection between the elevated beach platform to the north and no elevated beach platform to the south (Figure 5). We suggest that the Birch Bay magnetic contact reflects a concealed north-side-up fault, at least 24 km long, responsible for late-Holocene earthquakes and for the uplift of a beach platform immediately to its north.

4.2.2.2. Sandy Point Magnetic Contact

[24] A second northwest-striking magnetic contact extends from the Strait of Georgia, passes southeastward just south of Sandy Point (Figure 5, label SP) and then traverses southeast toward Bellingham Bay. Similar to the Birch Bay magnetic contact, the sense of the magnetic anomaly, with higher anomaly values north of the contact, is consistent with a north-side-up fault (Figure 5). The magnetic contact trends through the tip of Sandy Point (Figure 5), and therefore the zone of inferred uplift would include the coastal plain to the north. A series of uplifted late Holocene beach ridges are exposed on this coastal plain (see below), and the inferred north-side-up fault is consistent with coseismically uplifted beach berms on the Sandy Point coastal plain.

4.2.2.3. Drayton Harbor Magnetic Contact

[25] The Drayton Harbor magnetic contact extends ~25 km from Drayton Harbor to onshore regions (Figure 5, label DH). The magnetic contact has west-northwest strike through Drayton Harbor but rotates to an east-west trend farther east. At its eastern end, the Drayton Harbor magnetic contact appears to merge with a series of positive anomalies that extend east-northeastward to beyond the town of Sumas (Figure 5).
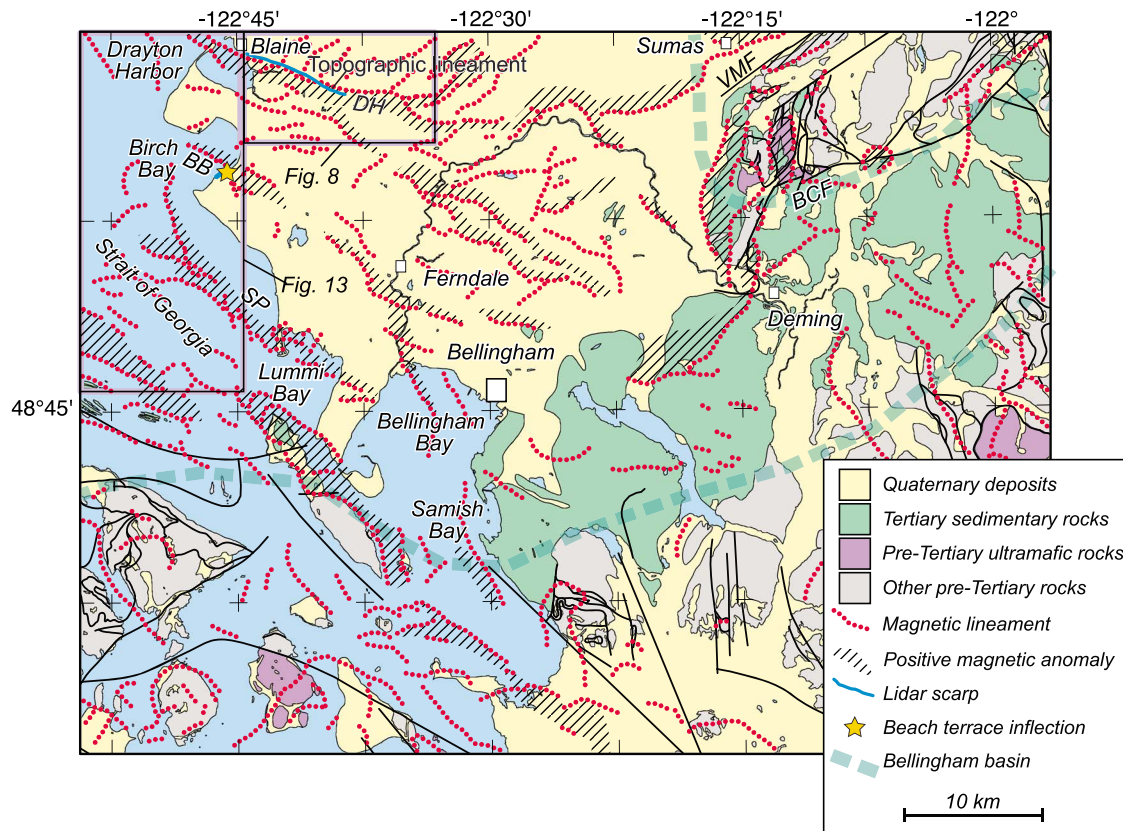
Figure 5. Interpretation of gravity and magnetic anomalies of the Birch Bay study area. Geologic map from *Dragovich et al.* [1997, 2002]. Red dotted lines are interpreted magnetic contacts. Black stipple indicates positive side of contact; i.e., the uplifted side of a fault, assuming normal polarity strata. Broad dashed line is margin of Bellingham basin, as shown in Figure 1. DH, Drayton Harbor magnetic contact; BB, Birch Bay magnetic contact; SP, Sandy Point magnetic contact; BCF, Boulder Creek fault; VMF, Vedder Mountain fault. Blue line near Blaine is topographic scarp observed in LiDAR data. Yellow star at Birch Bay is location of southern end of elevated beach platform.

[26] The northwest-striking magnetic contact through Drayton Harbor is roughly parallel to a topographic lineament (blue line, Figure 5) observed in LiDAR data (discussed below). The magnetic contact and topographic lineament are roughly parallel and proximal to each other, but their mapped positions are not precisely coincident, being off in some instances by 150 m or less.

5. Paleoseismic Investigations

5.1. Approach: LiDAR and Relative Sea Level Investigations

[27] We utilized high resolution digital elevation models, derived from LiDAR data sets, to evaluate evidence for surface displacement by Holocene faulting or folding. Two LiDAR data sets were utilized. The first is an early 2005 leaf-off survey of the Lummi reservation acquired by the Puget Sound LiDAR Consortium (http://pugetsoundlidar. ess.washington.edu) on behalf of the Lummi Nation (Figure 6). The design pulse density was >1 pulse/m². The second is a summer 2006 leaf-on survey over the remainder of western Whatcom County and western Skagit County acquired by the U. S. Geological Survey in cooperation with the Washington Department of Natural Resources and

Skagit and Whatcom Counties. The second survey had a pulse density of >0.5 pulses/m².

[28] Late Pleistocene and Holocene landforms are clearly visible on LiDAR images filtered to depict only bare-earth returns. Landforms associated with ice-margin processes, late Quaternary glacial runoff channels and glacial-isostatic-induced sea level changes [*Kovanen and Easterbrook*, 2002; *Kovanen and Slaymaker*, 2003] are common on the images. Superimposed on these ice-loading-related and glacial-process-generated landforms are three landforms that implicate Holocene faulting and folding: late Holocene uplifted beach storm berms (Sandy Point), uplifted late Holocene bay or estuarine flats (Birch Bay) and a topographic lineament extending east from Drayton Harbor that is defined by discontinuous south-side-up scarps (Drayton Harbor topographic lineament).

[29] Active coasts can provide useful information on active tectonics, and a standardized vocabulary is necessary to describe coastal neotectonic data. Relative sea level is the position of sea level relative to an arbitrary datum, in this case modern sea level. Evidence of abrupt relative sea level fall may be indicative of abrupt tectonically induced land-surface uplift. A storm berm is the highest beach berm along an active coast created by wave swash from storm waves; an
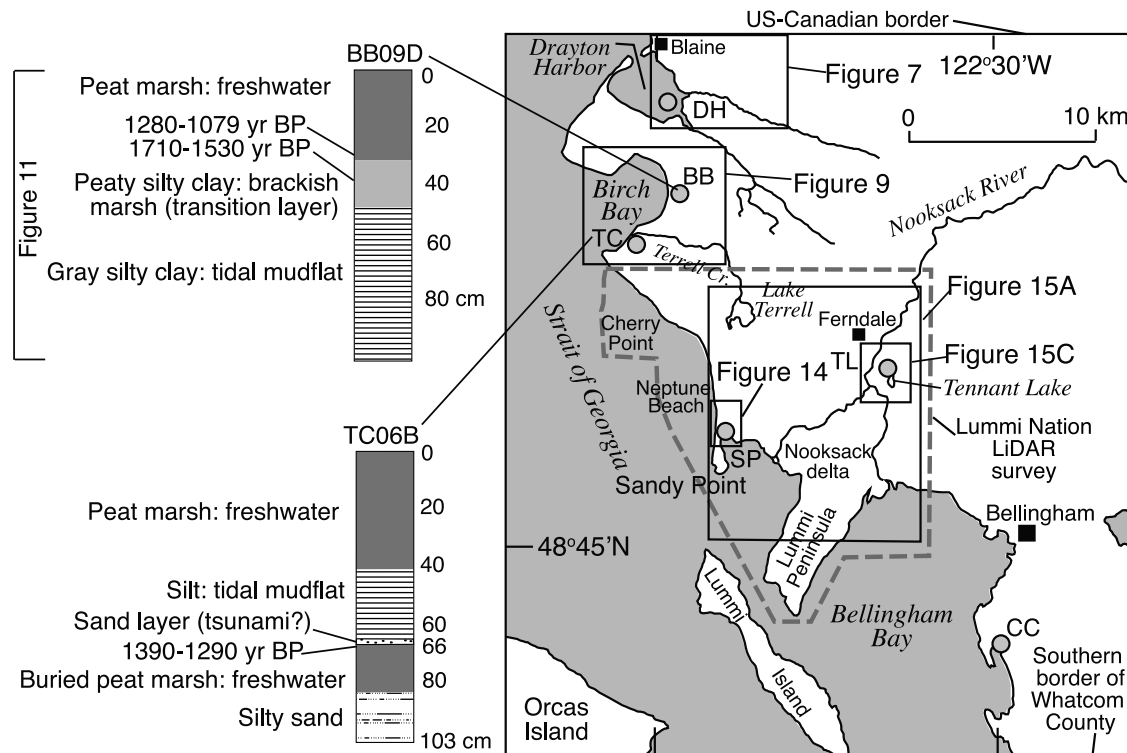
Figure 6. Map of western Whatcom county coast showing relative sea level paleoseismic study sites, core stratigraphy at selected sites, and bounds of the Lummi nation LiDAR survey. CC, Chuckanut Cove; TL, Tennant Lake; SP, Sandy Point; TC, Terrell Creek; BB, Birch Bay; DH, Drayton Harbor.

uplifted storm berm is a paleo-storm berm preserved by relative sea level fall. An uplifted Holocene shoreline is paleoshoreline preserved by relative sea level fall; the shoreline is defined by a beach cliff face that was cut by coastal erosion during the highest tides or storm waves. Finally, a beach platform defines a low gradient planated platform eroded in the surf zone; an uplifted beach platform is a platform preserved by relative sea level fall.

[30] Radiocarbon ages from coastal lowland deposits enable estimates of times of abrupt relative sea level change that we infer to be caused by earthquakes. All radiocarbon ages are on detrital wood, except a few instances where seeds were included (Table 3). Wood in all cases could be identified as small woody branches 3 mm or smaller in diameter and round in cross section. Commonly the branches had nodes where even smaller branches had been

Table 3. Radiocarbon Ages, Coastal Whatcom County

Sample ID[a]	Laboratory ID[b]	Date[c]	δ13C[d]	^{14}C Age[e]	Years BP[f]	Material
			Birch Bay			
BB09D29.5 (29.5–32 cm)	B-285333	10.12.10	−26.8	1260 ± 40	1280–1070	Six detrital wood twigs (3.0–6.5 mm long); one seed.
BB09D32 (32–33 cm)	B-285334	10.12.10	−27.4	2080 ± 40	2120–1900	Eight detrital wood twigs (2.0–9.0 mm long); one seed.
BB09D33 (33–34 cm)	B-285335	10.12.10	−26.8	2000 ± 40	2000–1830	Eight detrital wood twigs (2.0–9.0 mm long); one seed.
BB09D37B (37–39 cm)	B-274096	03.05.10	−28.2	2080 ± 40	2150–1940	Bulk peat sample.
BB09A40X (40–41 cm)	B-274095	03.05.10	−25.9	1700 ± 40	1710–1530	Three 2–3 mm-long wood frags, one 5-mm long needle, one 2 mm-diameter seed.
BB09D41 (41–42 cm)	B-274097	03.05.10	−27.4	1690 ± 40	1700–1520	Twenty 0.5–2.0 mm-long wood fragments.
			Terrell Creek			
TC06B66.5 (66.5 cm)	B-240535	02.28.08	−24.7	1430 ± 40	1390–1290	One wood stem detrital fragment, 18 mm long.
TC07C5076 (76–77 cm)	B-240537	02.28.08	nd	1500 ± 40	1510–1310	Five detrital wood fragments.
			Sandy Point			
SP06B43/43X (43–46.5 cm)	B-240534	02.28.08	−23.8	2180 ± 40	2320–2060	Two detrital wood fragments and 14 seeds.

[a]Sample code includes two-letter location identifier, last two digits of year sampled, letter designation for core, core depth in cm, subsample identifier.
[b]B, Beta Analytic.
[c]Run date, month.day.year.
[d]Delta 13C: 13C/12C ratio in o/oo; nd, not determined.
[e]Laboratory ^{14}C age, one standard deviation.
[f]Calibrated age range before CE 1950, 2 standard deviations, INTCAL04 [*Reimer et al.*, 2004]. 'Years BP' means years before CE 1950.

attached. All samples were delicate enough so the likelihood of recycling from an older deposit is small. Nonetheless, wood ages from the same horizon could range over 750 radiocarbon years (Table 3). Because samples are detrital, a resultant radiocarbon sample age indicates the maximum age of the sampled horizon. If more than one radiocarbon age determination was available from a stratigraphic horizon, we used the youngest age assuming the horizon could be no older than this youngest age. All calibrated age ranges are reported as "years BP," which means years before CE (current era) 1950 (Table 3).

[31] Relative sea level studies from multiple coastal sites, used conjunctively with LiDAR investigations, provide information on the timing and style of coastal deformation caused by late Holocene earthquakes [e. g., *Sherrod*, 2001; *Kelsey et al.*, 2008]. A primary assumption in using relative sea level to interpret coastal stratigraphy is that, within the northern Puget lowland, relative sea level has gradually been rising in the late Holocene [*Clague and James*, 2002; *James et al.*, 2009]. In a more detailed investigation of specific coastal marshes in the northern Puget lowland, *Beale* [1990] confirmed this assumption by finding that tectonically stable sites in the northern Puget lowland have submerged in the last few thousand years. If there is no vertical crustal displacement along the northwestern Washington coast, then the relative signal at all coastal localities should be the same and should record gradual submergence. We investigated the history of relative sea level at six sites where landforms and Holocene deposits collectively provide information on relative sea level change in the late Holocene (Figure 6).

[32] We first discuss the Drayton Harbor site (DH, Figure 6), where we employed a broad spectrum of approaches including analysis of LiDAR elevation models, ground magnetic surveys and relative sea level observations. However, the evidence for Holocene faulting remains questionable at this site. We next discuss the sites with evidence for Holocene faulting, which include Terrell Creek, Birch Bay and Sandy Point (TC, BB and SP respectively; Figure 6). We conclude with two sites with limited data, Tennant Lake and Chuckanut Cove (TL and CC; Figure 6), one having landform expression of recent relative sea level fall and the other a tectonically quiescent site with late Holocene gradual relative sea level rise.

5.2. Drayton Harbor Topographic Lineament and Scarp

[33] The Drayton Harbor topographic lineament, as mapped with LiDAR data, extends a minimum of 8 km from the town of Blaine and the northeastern part of the Drayton Harbor embayment east-southeastward subparallel to Dakota Creek. The topographic lineament is expressed both by topography and by disrupted drainage (Figure 7).

[34] The lineament is defined by discontinuous, linear up-to-the-south scarps (Figure 7) that cut across multiple drainages and as such do not appear to be erosional features. However, the scarps are discontinuous and in places hard to distinguish from subparallel fluvial features. The scarps are not the eroded edge of a major channel because the up-to-the south scarps are subparallel to up-to-the-north terrace risers on the northern side of the Dakota Creek valley. The scarps are notably more linear than the fluvial scarps of the minor streams that cut southward across them. Finally, the scarps

cut across different terrace levels. Where the up-to-the south scarps are well expressed, they could be fault scarps.

[35] To further assess whether the south-side-up scarps could be fault scarps, we acquired several key ground-magnetic transects across the Drayton Harbor topographic lineament where it manifests as a south-side-up scarp (Figure 8). Transects were conducted on foot using a cesium-vapor magnetometer integrated with GPS and carried in a backpack frame. Measurements were made at 1-s intervals while walking at normal speeds. A stationary proton-precession magnetometer was operated continuously to measure and correct for time-varying fields. The transects have been low-pass filtered at a 200-s cutoff.

[36] Magnetic profiles across the south-side-up scarp (Figure 8) closely mimic filtered aeromagnetic anomalies (Figure 4) and more precisely define the location of the magnetic contact. Each transect exhibits a sharp magnetic gradient, positive to the south and closely aligned with the magnetic contact numerically determined from the aeromagnetic data (Figure 5). Along the Valley View Drive transect (Figure 8; this transect is also depicted on the LiDAR image in Figure 7c), the magnetic field rises 135 nT from north to south over a distance of 540 m. The steepest gradient along Valley View Drive lies approximately 100 m south of the magnetic contact determined from aeromagnetic data and about 130 m north of the south-side-up scarp as observed in the field on Valley View Drive.

[37] Ground-magnetic and aeromagnetic data support the inference that the Drayton Harbor south-side-up scarp is the surface expression of a fault rather than being caused by erosion. We suggest that the ground-magnetic and aeromagnetic anomalies manifest concealed stratigraphy in the upper crust deformed by the same tectonic structure that is responsible for the topographic scarp. The magnetic lineament may reflect a fault that juxtaposes magnetic lithologies to the south, possibly pre-Tertiary rocks, against weakly magnetic Quaternary deposits to the north. The sense of the magnetic anomaly, with higher magnetic values south of the lineament, is consistent with south-side-up displacement of weakly magnetic, normally magnetized strata. Based on the amplitude and width of the steepest gradient along Valley View Drive, the top of the contact is located several hundred meters below Earth's surface. Although the magnetic and topographic lineaments are parallel to each other and proximal to each other, they are not coincident. The magnetic gradient is more sinuous than the scarp. The lack of coincidence may reflect complexities of the concealed deformation and its association with surface faulting. While the Drayton Harbor discontinuous, south-side-up scarps are a minimum of 8 km long, the magnetic contact along the north side of the magnetic high is 25 km long (Figure 5). Targeted trenching investigations across scarp segments will be required to strengthen the inference that the south-side-up scarps are fault scarps.

[38] Because one segment of the up-to-the-south Drayton Harbor topographic scarp is <1 km to the north of Drayton Harbor, we looked for an emerged marine deposit or landform fringing the north side of the harbor. However, there is no distinctive emergent landform on the inner (eastern) edge of Drayton Harbor. The mudflat at Drayton Harbor (site DH, Figure 6) is underlain at shallow depth (within a meter) by glaciomarine drift, and the distinctive large boulders that
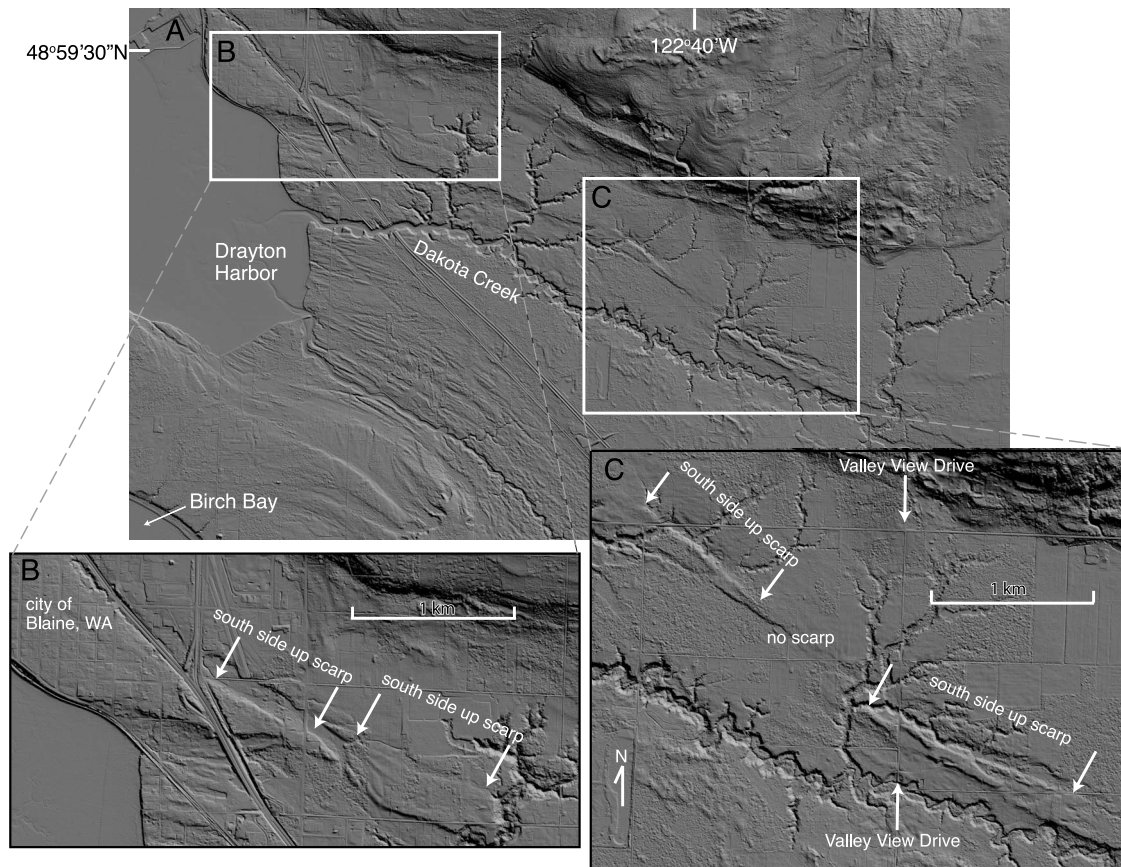
Figure 7. (a) LiDAR hillshade image showing Drayton Harbor topographic lineament consisting of south-side-up scarp segments. (b) A two-km-long, south-side-up scarp east of Blain, Washington; the scarp is cut through by the middle by a southeast-directed channel that was diverted eastward along the scarp. (c) Two scarp segments 1.0 and 1.5 km long, with intervening region of no scarp. For both scarp segments, a southwest-flowing drainage is diverted westward along the scarp face. For the eastern side of the two scarp segments, the linear south-side-up scarp cuts across and similarly offsets two different levels of fluvial terraces. Location of Figure 7 depicted in Figure 6.

litter the mudflat surface at low tide are winnowed from the glaciomarine drift as the drift is eroded by coastline retreat. The mudflat at Drayton Harbor provides an inconclusive relative sea level trend.

5.3. Abrupt Subsidence at Terrell Creek Marsh

[39] The Terrell Creek marsh is situated landward of a beach berm within the estuarine reaches of lower Terrell Creek (TC, Figure 6; Figures 9 and 10). The marsh is inset within a valley bounded by terraced Pleistocene glacial deposits ('upland' in Figure 9b).

[40] Within the Terrell Creek estuarine lowland, multiple (n = 21) cores over the length and width of the marsh (Figure 9b) revealed four common attributes. First, the surface layer of the marsh (uppermost 35–40 cm) consists of freshwater peat that grades downward to a gray to brownish gray mud; second, an abrupt lithologic transition in the upper meter, at about 0.6 m depth, from a buried black peat soil upward to the gray to brownish gray mud occurs in all cores; third, at the contact of the buried peat soil and overlying mud is a 1-mm-thick, fine-to-very-fine sand; and fourth, the mud at ~1.4 m depth contains estuarine shells.

[41] Timing and nature of the environmental change that occasioned burial of the black peat soil indicate the change was caused by sudden submergence. Diatom biostratigraphic data for core TC06A (Appendix), obtained by sampling across the upper contact of the buried peat, indicate that the site changed abruptly from a peaty freshwater marsh to a tidal mudflat.

[42] We sampled the Terrell Creek buried peat for radiocarbon age determination in two cores (TC06B66.5 and TC07C5076, Figure 6 and Table 3). Radiocarbon ages of the two samples overlapped, and the youngest ^{14}C age, on a single branch that was exactly at the buried soil contact, yielded a calibrated age of 1390–1290 years BP (Figure 6, Table 3). We interpret the age range of 1390–1290 years BP to be the best estimate of the time of abrupt submergence of the Terrell Creek marsh.

[43] From our coring program that consisted of 21 cores in three transects over the length and width of the marsh (Figure 9b), we infer the Terrell Creek estuary abruptly subsided in the late Holocene and that submergence was long lasting. Uniform abruptness of contacts above the buried soil indicates rapid submergence allowing tidal inundation of the marsh and deposition of tidal sediment.
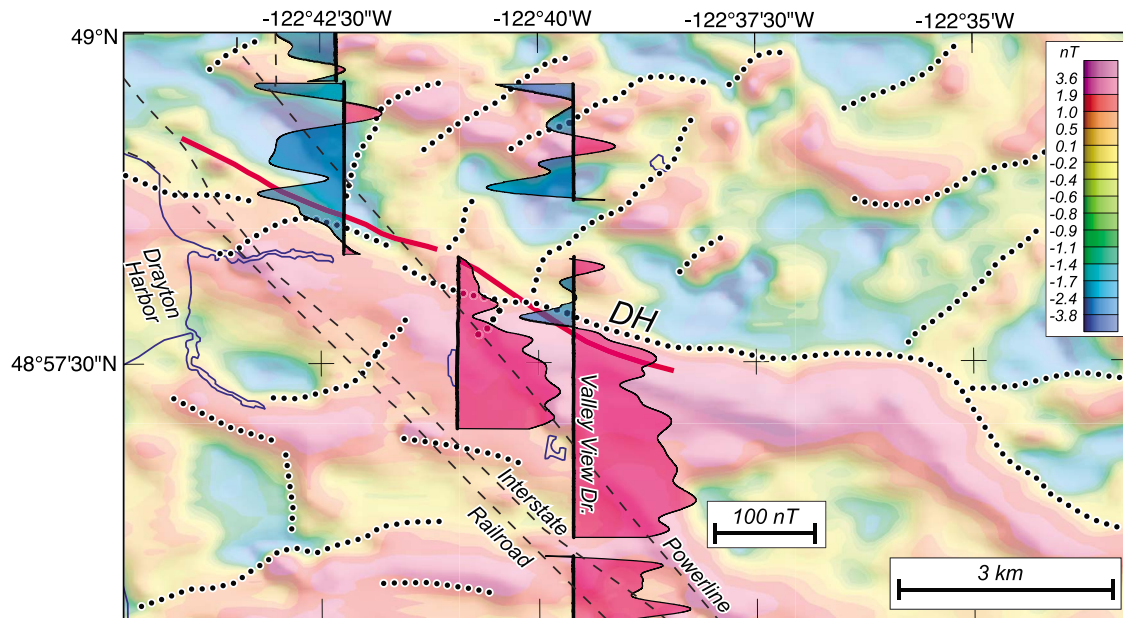
Figure 8. Ground-magnetic profiles across the Drayton Harbor scarp. Red lines indicate LiDAR scarp. Bold black lines are location of magnetic transects; positive and negative anomalies shown in red and blue, respectively, relative to an arbitrary datum. Ground-magnetic anomalies have been low-pass filtered; see text for explanation. Base map shows aeromagnetic anomalies, filtered in order to emphasize shallow sources. Black dotted lines are magnetic contacts determined directly from airborne magnetic anomalies. Location of Figure 8 depicted in Figure 5.

Submergence was long lasting as indicated by the 25 cm of mud that accumulated above the buried soil. From core coverage, we document that the abrupt subsidence event affected the entire marsh and local estuarine area. We infer that the abrupt subsidence was a tectonic response to an earthquake. Subsequently, the site gradually re-emerged to host a peaty freshwater wetland again.

[44] The 1 mm-thick sand deposit at the contact between the abruptly subsided freshwater peat and the overlying tide flat mud (e.g., core TC06B, Figure 6; see location of this core on Figure 9) was present in most of the 21 cores that we described across the Terrell Creek estuary. Following observations of *Witter et al.* [2003] and *Cisternas et al.* [2005] that document tsunami sand overlying subsided wetland soils on tectonically active coasts, we infer that the sand was transported to the Terrell Creek estuary by a tsunami triggered by the earthquake that caused coseismic subsidence of the Terrell Creek marsh.

5.4. Emerged Estuary at Birch Bay: Abrupt Vertical Crustal Displacement in the Late Holocene

[45] The Birch Bay coastal plain (Figure 9a) is three to four meters above mean lower low water (Figure 10), and the town of Birch Bay sits on the modern beach berm at the seaward end of this plain. Terrell Creek estuary sits within an incised valley 3 km to the south of the Birch Bay coastal plain. Preexisting seismic reflection investigations [*Hurst*, 1991] indicate that an anticline with possible Quaternary activity underlies the coastal plain at Birch Bay (Figure 1d). From our reconnaissance coring at Birch Bay, we hypothesized that the Birch Bay area experienced one abrupt uplift event in the late Holocene that raised a tide flat above modern high tide levels. We evaluate this hypothesis.

5.4.1. Stratigraphy at Birch Bay

[46] We investigated the Birch Bay coastal plain (site BB, Figure 6) with a suite of 12 cores (Figure 9a) and follow-up radiocarbon dating and biostratigraphic investigation. The stratigraphy beneath the Birch Bay coastal lowland consists, within the upper meter, of a gray mud overlain by peat (Figures 6 and 11). The mud-to-peat transition is initially gradual and then abrupt. The root-rich silty clay transition layer is 13–19 cm thick, and an abrupt change to fibrous peat occurs at the top of the transition layer (Figure 11). We undertook detailed diatom biostratigraphic investigation in the transition interval.

[47] Radiocarbon sampling of core BB09D (core location in Figure 9) chronicles the mud-to-peat transition. The lower portion of the rooted silty clay transition layer, at 40–41 cm core depth, yields an age range of 1710–1530 years BP (Table 3), which indicates that the tide flat was partially emergent by this time. The sample interval 29.5–34 cm chronicles the upper abrupt transition to peat and yields an age range of 1280–1070 years BP (the youngest of three ages in this interval, see Table 3), indicating that Birch Bay abruptly changed to a peaty coastal plain by at least 1280–1070 years BP.

[48] By comparison, the Terrell Creek estuary abruptly subsided in the age range 1390–1290 years BP. Given that the sample material in both cases is delicate detrital branches that provide maximum-limiting ages (oldest possible age), the closely similar age ranges (1390–1290 versus 1280–1070 yr BP) are not inconsistent with the inference that the final sudden emergence at Birch Bay was coincident with the abrupt submergence at Terrell Creek. Employing the youngest age range as the most likely time of the earthquake, we infer that the latest Birch Bay earthquake, which
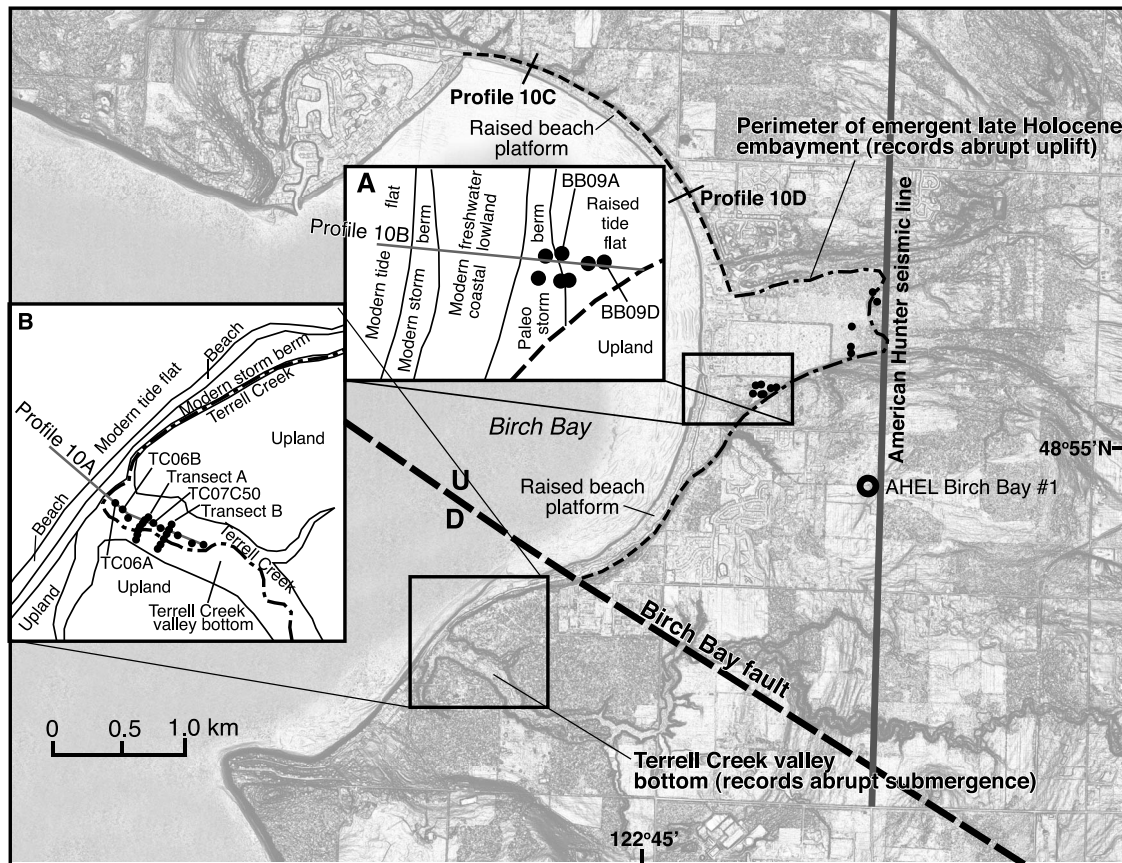
Figure 9. Image of Birch Bay showing (a) Birch Bay and (b) Terrell Creek paleosesismic sites. Image is a LiDAR-based slope map with a histogram weighted gray scale color model. The two inset maps show core transects in the Birch Bay coastal plain and the Terrell Creek valley bottom. Black dots are individual core sites. Dashed line delineates the inland edge of the uplifted Holocene shore platform. Dashed-and-dotted line shows the extent of the uplifted embayment. Bold dashed line depicts best approximation of the trace of the Birch Bay fault, which is blind at the surface, separating Holocene subsidence (D) from Holocene uplift (U). Location of Figure 9 depicted in Figure 6.

occasioned the final sudden emergence at Birch Bay and the abrupt submergence at Terrell Creek, occurred 1280–1070 years BP or within a century thereafter.

5.4.2. Diatom Biostratigraphy and Environmental Change at Birch Bay

[49] We reconstructed paleoelevation and paleosalinity from a suite of stratigraphic samples using quantitative diatom paleoecology (i.e., calibration). Our technique relied on statistical comparisons between modern and fossil diatom assemblages, the results of which allow us to investigate past sea level changes at Birch Bay in detail. For our modern database, we collected multiple surface sediment samples from each of seven coastal wetland sites in the northern Puget lowland (Figure 1). At each modern sample location, we measured elevation and salinity. For elevation, we leveled all stations to USGS benchmarks, or the highest tide of the day, and tied the leveled elevations to tide gauge observations at the closest tide stations to obtain elevation relative to local tidal datums. We measured salinity with an optical refractometer.

[50] For fossil samples from Birch Bay, we used a 74-cm long core collected with a 5 cm-wide gouge corer. In the laboratory, we described lithostratigraphic changes in the

core and collected 1 cm^3 subsamples every 5 cm between depths of 5–25 cm, every 2.5 cm between 25–33 cm, and ~5 cm intervals between 58–74 cm in depth. We targeted stratigraphic changes observed between 33 and 54 cm in depth with 1- cm^3 subsamples collected every 1 cm.

[51] For modern samples, we counted and identified at least 300 diatom valves under oil immersion, and for all but one of the fossil samples, we counted at least 400 valves. A core sample from 5.6 cm in depth contained a poorly preserved diatom assemblage and we only counted 118 valves in that sample. We included fragments of more than half of a diatom valve in the counts. See Appendix for mounting technique for permanent microscope slides diatom analysis.

[52] Because elevations of our modern diatom sample sites differ with respect to tidal range [see *Zong and Horton*, 1999], our elevations relative to local tidal datums were standardized relative to mean higher high water (MHHW) by a standardized water level index:

$$SWLI_X = ((ELE_X - MTL)/(MHHW - MTL) * 100) + 200$$

where $SWLI_X$ is the standard water level index for sample X, ELE_X the elevation of sample X, MTL the mean tidal
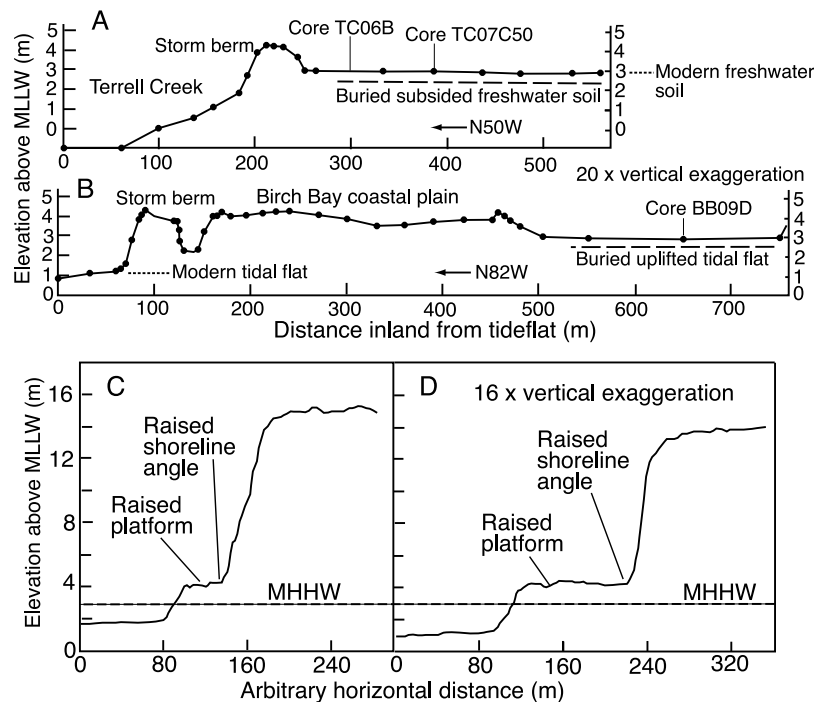
Figure 10. (a) Shore perpendicular survey profile at Terrell Creek estuary. (b) Shore perpendicular survey profile at Birch Bay coastal plain. Both shore perpendicular survey profiles show modern topography and elevations of vertically displaced stratigraphic horizons. (c, d) Topographic profiles across the raised beach platform on the shoreline at Birch Bay. For all profiles, elevation datum is MLLW (Mean Lower-Low Water). See Figure 9 for locations of profiles 10a, 10b, 10c, and 10d. Profiles 10a and 10b are constructed from digital level surveys with survey closure error of <10 mm; profiles 10c and 10d are constructed from a DEM configured from the LiDAR database (approximately 20 cm vertical resolution). MHHW, Mean Higher-High Water.

level at the sampling site and MHHW the higher high water level at the sampling site. The addition of a constant (200) ensures that all SWLI values within the training set are positive. SWLI values computed in our calibration analysis are then converted back to MHHW level at the sampling site by reverse calculation of the SWLI equation.

[53] To reconstruct paleoelevation and paleosalinity, we employed multivariate statistical techniques using the modern surface sediment diatoms assemblages and our fossil diatom assemblages from the Birch Bay core (BB09D). Calibration of SWLI and salinity was done using unimodal distribution models (weighted average (WA) and weighted averaging partial least squares (WA-PLS)). We employed the C2 program for our calibration [*Juggins*, 2003] and excluded taxa with abundances of <2% from the statistical analysis. Calculated statistical parameters are the coefficient of determination (r^2) and root mean square error of prediction (RMSEP). Both parameters measure the strength of the relationship between observed and inferred environmental values [*Birks*, 1995]. Model selection is based on a low RMSEP and high r^2. We applied these models to our fossil assemblages to give sample-specific reconstructions of SWLI and salinity.
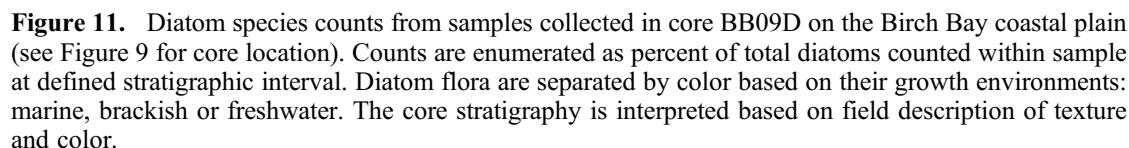
[54] We also use the modern analogue technique (MAT) within C2 to identify fossil samples that have 'poor' modern analogs when compared to the modern data set [*Juggins*, 2003; *Birks*, 1995; *Zong et al.*, 2003]. We define a good modern analog as having a minimum dissimilarity

coefficient value greater than the upper 20th percentile threshold of the data set. This is important because calibration models are less reliable for fossil samples that have poor modern analogs in the modern database.

[55] Within the core BB09D, there are three biostratigraphic units, diatom zones 1, 2 and 3 (Figure 11). Diatom zone 1 is in the lower part of the core (Figure 10) and is dominated by marine diatoms - mostly *Scoleoneis tumida*, *Gyrosigma balticum*, *Grammatophora oceanica*, and *Paralia sulcata*. Diatom zone 1, with the upper limit at 44 cm depth, corresponds to the gray mud in Figure 11 and to the silty clay of core BB09D in Figure 6.

[56] Diatom zone 2 is between 44 and 33 cm depth and consists of both marine and brackish diatoms (Figure 10). This zone is dominated by several diatoms including *Diploneis interrupta* (marine/brackish), *Paralia sulcata* (marine), *Aulacoseira italica* (low salinity brackish to freshwater), *Tabellaria fennestrata* (freshwater), *Pinnularia viridis* (freshwater), and *Eunotia praerupta* (freshwater). The dominant diatoms, representing a mixture of marine, marine/brackish and freshwater affinities, together define a brackish marsh environment, which is ideal for brackish marsh diatom floras.

[57] Diatom zone 3 is in the upper 33 cm of the core and is dominated by freshwater diatoms (Figure 10). The diatom zone floras were poorly preserved, but the floras are typical of shallow-water freshwater marsh environments similar to

Figure 11. Diatom species counts from samples collected in core BB09D on the Birch Bay coastal plain (see Figure 9 for core location). Counts are enumerated as percent of total diatoms counted within sample at defined stratigraphic interval. Diatom flora are separated by color based on their growth environments: marine, brackish or freshwater. The core stratigraphy is interpreted based on field description of texture and color.

freshwater marsh diatom floras observed on the Birch Bay coastal plain today.

[58] From the vertical distribution of diatom flora within the core BB09D (Figure 10), there are two transitions that separate three diatom zones (Figure 11). Most of the brackish marsh flora appear abruptly at the lower transition at 44 cm depth (the mud-peat contact), and several brackish aerophiles (soil diatoms) appear only in this part of the core. The upper transition (from zones 2 to 3) at core depth 33 is where the brackish diatoms suddenly disappear and the flora become virtually all freshwater diatoms (Figure 11).

[59] Reconstruction of elevations and salinity from diatoms [*Birks*, 1995; *Hemphill-Haley*, 1995; *Juggins*, 2003] (Figure 12) provides estimates of amount of relative sea level fall based on diatom abundances in modern and fossil assemblages. Stratigraphic indications of relative sea level fall, based on diatoms, commence at 52 cm core depth in core BB09D, and indications of relative sea level fall persist upwards in the core until 33 cm core depth (Figure 11). Comparison of marine mud to overlying freshwater peat based on environmental reconstruction (Figure 12) shows paleoelevation differences of at least 0.5 m and as much as 2.0 m. The comparison indicates the site rose (that is, relative sea level fell) by at least 50 cm and may have risen by as much as 2 m (Figure 12).

[60] We infer that tectonically induced land-level changes caused the relative sea level fall at Birch Bay. The late Holocene non-tectonic relative sea level signal is a gradual relative sea level rise [*Beale*, 1990; *James et al.*, 2009]; therefore any abrupt relative sea level fall is likely tectonic in origin. The transition from brackish to freshwater environment was abrupt and resulted in emergence of a tide flat. Only a tectonic land level change could have induced such emergence. Strengthening the inference that the abrupt Birch Bay uplift was tectonic in origin is the apparently coincident subsidence at the adjacent Terrell Creek site 3 km to the south.

[61] The stratigraphic relations depicted in the survey profiles in Figure 10 support as much as 2 m of vertical displacement associated with coseismic deformation in the Birch Bay-Terrell Creek coastal area. The surveyed profiles show that the buried freshwater soil at Terrell Creek estuary is at least 0.5 m below the modern equivalent soil. Similarly, the buried uplifted tidal flat at Birch Bay is on the order of 1.5 m above the modern equivalent tidal flat (Figure 10). These observations support the inference from diatom observations that the vertical displacement associated with the fault slip that displaced Birch Bay relative to Terrell Creek was at least 0.5 m and may have been as much as 2 m.

5.4.3. Birch Bay Fault

[62] We infer that a buried fault between Birch Bay and Terrell Creek (Figure 9) accommodated the synchronous uplift and subsidence. The fault tip must be buried because there is no scarp in the region where the fault would intersect the ground surface (Figure 9).

[63] Deformation associated with this fault was complex because, based on diatom observations, the Terrell Creek site appears to have coseismically subsided all at once, while the Birch Bay site appears to have uplifted gradually at first and then culminated in an abrupt coseismic uplift. Although
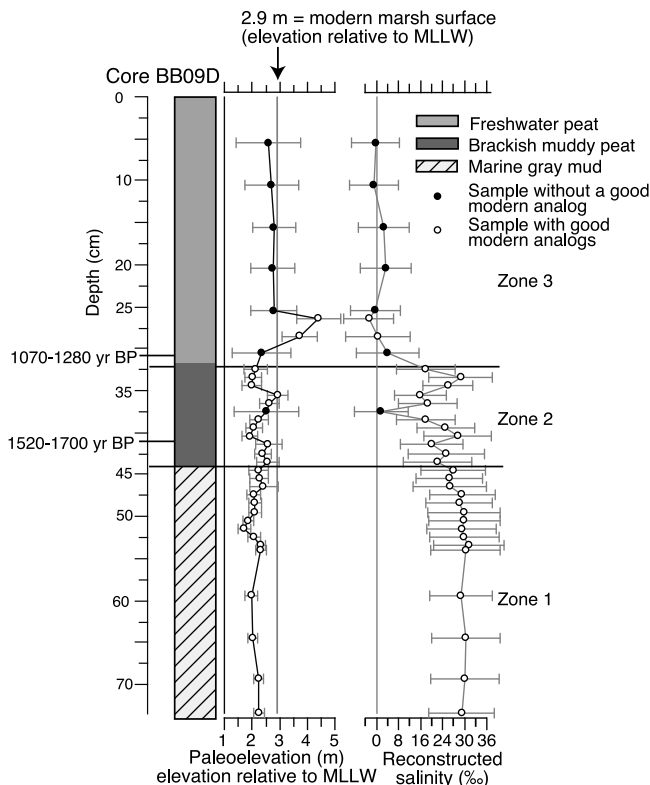
Figure 12. Reconstructed paleoelevations relative to mean lower low water (MLLW) and reconstructed salinity for samples from core BB09D that was collected on the Birch Bay coastal plain. Error bars are ±1 standard error. See Figure 9 for core location.

the fault deformational mechanism is unclear, what is clear is that the coastal geomorphology requires only one uplift event (one abrupt drop in relative sea level). In order to satisfy both the geomorphic observations at Birch Bay and the diatom paleo elevation estimates for the Birch bay area, we suggest initial slow slip resulted in contraction of the anticline (Figure 1d) and consequent gradual uplift, and then coseismic slip both further uplifted the Birch Bay coastal plain and simultaneously submerged the lower Terrell Creek valley.

[64] The flat elevated coastal plain inland of the Birch Bay beach berm, which we infer is a raised beach platform, constrains the north-to-south width of the region of coseismic uplift in the hanging wall during the last earthquake. This platform is 1.3–1.0 m above modern mean higher high water (Figures 10c and 10d). The southern extent of the raised beach platform that fringes Birch Bay (Figure 9) is the southern extent of coseismic uplift on the coast, and this south edge of the raised platform likely delineates where the buried fault crosses the coast. Because the northern extent of the raised platform is 4 km to the north of the coastal location of the buried fault (Figure 9), we infer the north-to-south width of the coseismic uplift to be on the order of 4 km.

5.4.4. Detailed Marine Magnetic Survey of Birch Bay and Surrounding Areas

[65] Magnetic data help define the east-to-west lateral extent of the Birch Bay fault both shoreward and seaward. A prominent northwest-striking magnetic anomaly is apparent

in airborne magnetic data (Figure 4 and Figure 5, label BB) crossing Birch Bay and extending onshore for several kilometers. The anomaly occurs at the inferred trace of the Holocene Birch Bay fault, separating the uplifted coastal plain at Birch Bay from the subsided marsh at Terrell Creek (Figure 9). The southwestern margin of the Birch Bay magnetic anomaly coincides closely with the southern limit of the uplifted beach platform at Birch Bay (Figure 9), and thus the anomaly may reflect uplifted, slightly magnetic stratigraphy in the subsurface. If so, the magnetic anomaly allows us to map the location of the uplift both northwest and southeast of the beach platform. To understand the Birch Bay magnetic anomaly in greater detail, we conducted a detailed magnetic survey of Birch Bay and surrounding marine areas (Figure 13).

[66] The marine-magnetic survey was conducted with a 5-m-long fishing boat powered by a single outboard motor and navigated with GPS. The boat was constructed of fiberglass and aluminum and thus was essentially nonmagnetic. The motor did produce a small magnetic field, however, which was minimized by positioning the magnetic sensor, a cesium-vapor magnetometer, at the end of a 3.4-m-long wooden pole extending forward from the bow of the boat. Overall, the magnetic field of the boat and motor produced a maximum heading error of 13 nT, which was removed from the data using a standard heading correction. A proton-precession magnetometer was stationed at a fixed location nearby and operated during the entire survey in order to measure and subsequently remove diurnal and transient magnetic fields. Total-field anomalies were computed by subtracting the International Geomagnetic Reference Field on the days of the survey. The marine survey was conducted along northeast-directed track lines spaced 500 m apart (Figure 13). Four northwest-directed tie lines were included to check for cross-track consistency. After heading corrections were made, the 56 crossings of tie lines and track lines had an average absolute crossing error of 0.06 nT, approximately 0.6 percent of the total-field at each crossing.

[67] It is evident from Figures 4 and 13 that magnetic anomalies seen in aeromagnetic data, when filtered in order to emphasize shallow magnetic sources, are also present in ocean-surface measurements. While this is not a surprising observation, it clearly demonstrates that our filtering methodology applied to aeromagnetic data is useful in illuminating near-surface lithologies and tectonic structures. The magnetic field in marine areas surrounding Birch Bay is dominated by northwest-striking anomalies, possibly reflecting folded and faulted lithologies in the near surface. The Sandy Point magnetic anomaly (Figures 5 and 13, label SP) extends across the entire marine survey, and the Birch Bay anomaly (Figures 5 and 13, label BB) extends entirely across Birch Bay.

[68] The southwestern margin of the Birch Bay magnetic anomaly coincides with the southern margin of the uplifted beach platform that is depicted in Figure 9, suggesting that the anomaly is caused by slightly magnetic stratigraphy raised closer to the earth's surface by uplift on the Birch Bay fault. To further illuminate this contact, we also conducted a ground-magnetic transect around the Birch Bay shoreline (Figure 13). The transect was walked during low tide and as far west as possible in order to minimize cultural noise from the local community. A pronounced 50-nT positive anomaly
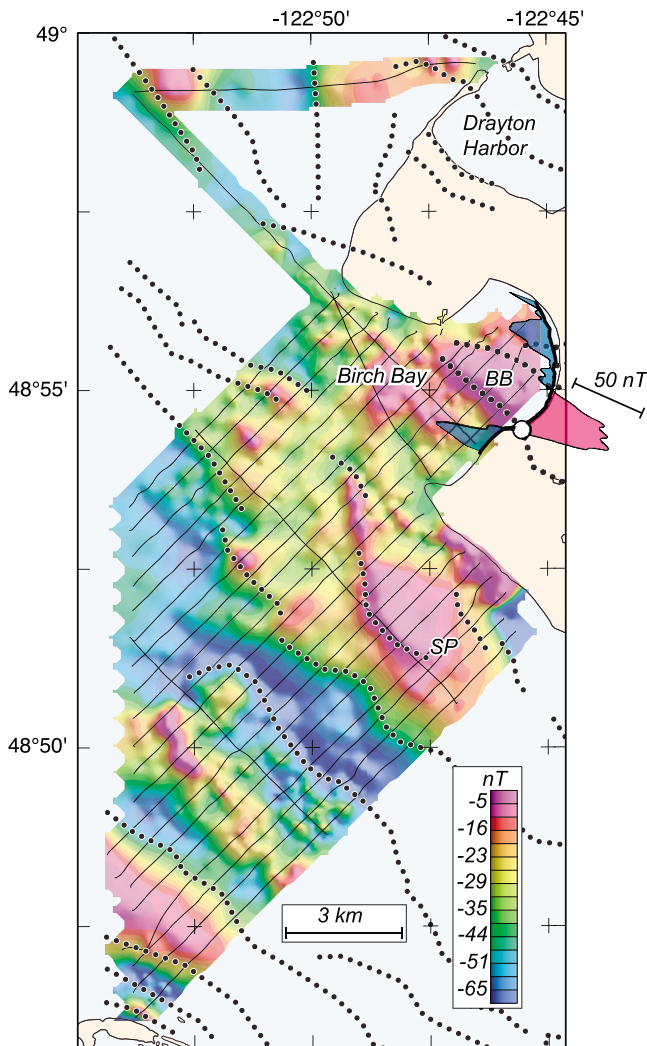
Figure 13. Marine-magnetic survey and ground-magnetic transect of Birch Bay. Thin black lines show location of track and tie lines. Black dotted lines are magnetic lineaments interpreted from aeromagnetic data. The bold black line around Birch Bay indicates the location of a ground-magnetic transect; red is positive and blue is negative relative to an arbitrary datum. White circle is southern margin of uplifted beach terrace. BB, Birch Bay magnetic contact; SP, Sandy Point magnetic contact. Location of Figure 13 depicted in Figure 5.

was observed on the transect (Figure 13), consistent with the airborne and marine magnetic data. The sharp gradient at the southern margin of the anomaly is located at the southern margin of the uplifted beach platform, consistent with a north-side-up fault at this location.

[69] The Birch Bay magnetic contact does not appear to extend northwest beyond Birch Bay, suggesting either that the causative structure is confined to Birch Bay or that it loses its magnetic properties beyond Birch Bay. On the other hand, Figure 4 indicates that the Birch Bay magnetic contact does extend southeastward from the shoreline for several kilometers, where it is completely obscured by magnetic fields associated with a paper mill and aluminum smelter. The Birch Bay magnetic contact thus defined, from Birch

Bay to the paper mill, is only about 5 km in length. However, a linear, northwest-striking magnetic anomaly is located southeast of the paper mill and aluminum smelter and is on strike with the Birch Bay magnetic anomaly (Figure 5). This magnetic feature extends to a point about midway between Ferndale and Bellingham. We suggest that the northwest-striking lineament between Ferndale and Bellingham is the continuation of the Birch Bay magnetic contact (Figure 5). Viewed in this way, the Birch Bay magnetic contact, and by inference the Birch Bay fault, extends from the northwestern edge of Birch Bay to north of Bellingham, a total distance of 24 km. We use this fault length in moment magnitude calculations below.

5.5. Paleoseismology of the Coastal Plain at Sandy Point

[70] Sandy Point (site SP, Figure 6; Figure 14) is a sand spit developed at the south end of a raised coastal plain, the Sandy Point coastal plain. The east side of the Sandy Point coastal plain is banked against a Holocene-age paleo-sea cliff (Figure 14a). Late Pleistocene shorelines are notched in the hillslopes 12 to 30 m above the paleo-sea cliff (Figure 14a). The late Pleistocene shorelines were cut while relative sea level fell during glacio-isostatic rebound. At the latitude of Vancouver, British Columbia (only 25 km to the north), isostatic rebound was largely completed by 8000 yr BP and thereafter sea level tracked the Holocene eustatic curve for Northern Hemisphere midlatitudes [*Clague and James*, 2002; *James et al.*, 2009]. The Sandy Point coastal plain developed by southward longshore sand drift after the cessation of rapid relative sea level rise in the mid Holocene.

5.5.1. Shoreline Morphology at South End of Sandy Point Coastal Plain

[71] Three abandoned shorelines are visible on LiDAR imagery (Figure 14b) at the south end of the Sandy Point coastal plain. A north-trending transect (surveyed with a digital level, closure error 1 mm) across the south end of the Sandy Point coastal plain (transect X-Y, Figure 14c) shows three abandoned surfaces ('Uplifted tide flats', Figure 14c), each terminating at the seaward end in an abandoned shoreline.

[72] We excavated and described stratigraphy in a soil pit across the middle abandoned surface (SP06B, Figure 14c). Diatom investigations of a soil monolith from pit SP06B (Appendix) indicates an abrupt upward transition from tide flat to a freshwater environment at 40 cm depth. The elevation of the top of the paleo-tide flat underlying the middle abandoned surface is higher than modern mean high water (MHW, Figure 14c), which is consistent with uplift of the shoreline and associated paleo-tide flat. Based on similar stratigraphy underlying the three abandoned surfaces, we infer that all three abandoned surfaces are underlain by uplifted tide flat deposits (Figure 14c).

5.5.2. Three Episodes of Abrupt Relative Sea Level Fall at Sandy Point

[73] Based on the presence of three uplifted tide flats surfaces, we infer that three late Holocene shorelines on the sand spit at Sandy Point (yellow, green, purple: youngest to oldest; Figure 14b) are preserved because of three instances of abrupt relative sea level fall. The oldest shoreline is preserved near the eastern edge of the Holocene platform
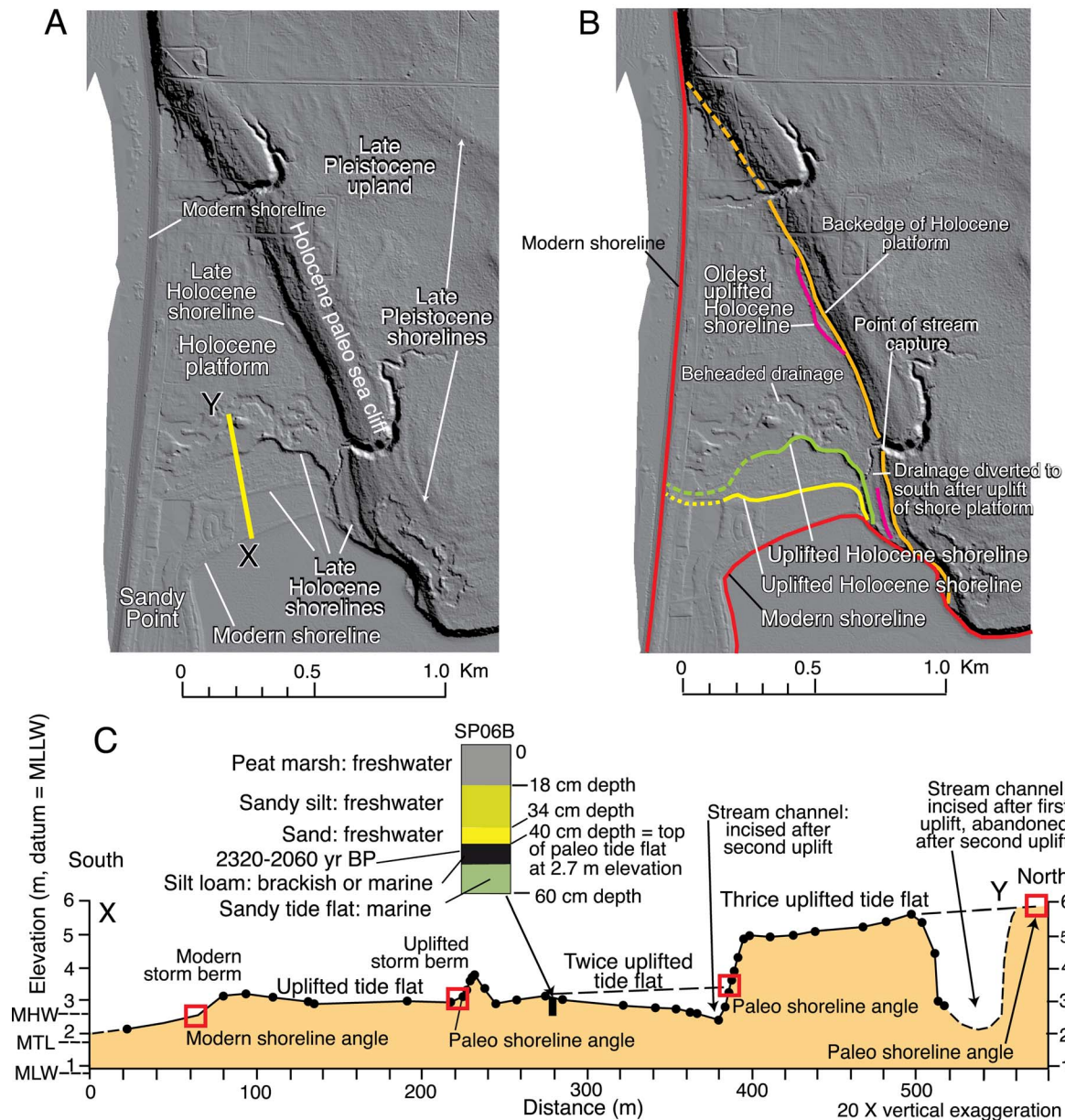
Figure 14. (a) LiDAR image of Sandy Point coastal area delineating late Pleistocene and Holocene landscapes and preserved shorelines. Location of Figure 14 depicted in Figure 6. (b) Same LiDAR image as A. but delineating a set of uplifted late Holocene shorelines (yellow, green, purple; youngest to oldest). Also shown on the Holocene platform is an abandoned, beheaded drainage and the point of stream capture. The capture was caused by headward growth of a south-flowing tributary whose gradient was increased by a drop in base level after uplift of the green shoreline. (c) Surveyed cross section across the modern and three paleo-tide flats, using digital level. Survey closure error = 1 mm. Elevation datum is MLLW. Surveyed ocean level tied to NOAA tide station 9449424 at Cherry Point, WA. MLLW, Mean Lower-Low Water. MLW, Mean Low Water. MTL, Mean Tide Level. MHW, Mean High Water. Red squares depict the location and elevation, within 0.5 m, of the modern shoreline angle landward of the modern tide flat and the three paleo-shoreline angles for the three uplifted tide flats. Elevation of shoreline angles derived from surveying, except for the elevation of the oldest paleo-shoreline angle that is approximated from the Lummi Bay 7.5′ topographic map. The elevation of top of the paleo-tide flat in the excavated pit (SP06B) is 2.7 m relative to modern MLLW.

adjacent to the paleo-sea cliff. The younger two shorelines are preserved at the south end of the Sandy Point coastal plain (Figure 14b).

[74] Abrupt relative sea level fall caused drainage disruption on the coastal plain. The oldest of the younger two shorelines (depicted in green, Figure 14b) was abandoned by relative sea level fall shortly before a south-flowing coastal stream captured the headwaters of a larger stream that flowed westward across the uplands and across the Holocene platform to the Strait of Georgia. Uplift of the shoreline lowered the base level of the stream, causing headward erosion that captured and beheaded the stream flowing off the upland. As a consequence, the beheaded west-flowing drainage on the platform was abandoned (Figure 14b).

[75] Because Puget lowland late Holocene relative sea level change in the absence of tectonic input is gradual submergence [Beale, 1990], we infer that the three tide flat surfaces were raised by uplift during three earthquakes. From surveyed transect elevations (Figure 14c), we estimate uplift amounts from the differences between the elevations of the shoreline angles (the platform-sea cliff junction, depicted by the red squares in Figure 14c) for each adjacent uplifted tide flat. Based on shoreline angle elevations, the younger two raised tide flats each appear to have been uplifted by a meter or less during two separate earthquakes. A sample of 14 seeds and two small branches within the top of the buried tide flat deposit from the next-to-youngest raised tide flat has an age of 2320–2060 years B. P. (log of excavation SP06B, Figure 14c) (Table 3), from which we infer that the youngest coseismic uplift occurred after about 2,100 years ago. The oldest of the three raised tide flats appears to have been uplifted 2.0–2.5 m during the earliest recorded earthquake. The oldest raised tide flat has been cumulatively uplifted about 4 m (Figure 14c) during three late Holocene earthquakes.

[76] The fault that occasioned coseismic uplift of the shorelines may be coincident with the structure responsible for the Sandy Point magnetic contact (Figure 5). The uplifted shorelines are north of the Sandy Point magnetic contact, which is consistent with weakly magnetic strata juxtaposed in an up-to-the-north sense.

5.6. Stratigraphy and Geomorphology at Tennant Lake

[77] Stratigraphy beneath the Tennant Lake marsh (site TL, Figure 6; Figure 15) consists of peat to peaty silt underlain by a strath surface (0.7–2.5 m depth) cut on late Pleistocene glaciomarine drift. A sand deposit, 2–5 cm thick, lies on top of the strath (Figure 15e).

[78] A riser lies north of the Tennant Lake marsh, where it separates the marsh and surrounding deltaic environs from an elevated floodplain of the Nooksack River. The riser is evident on LiDAR imagery ("Riser separating emergent delta from floodplain," Figure 15d) but not in aeromagnetic data.

[79] We did little work at this site; however, the geomorphology (the riser, Figure 15d) and the stratigraphy (Figure 15e) in conjunction argue for an uplift interpretation. Beach sand deposited on a strath cut on glaciomarine drift, which was backed by a sea cliff, was uplifted relative to sea level. The uplift occasioned both deposition of a coastal lowland peat on top of the beach deposit and abandonment of the sea cliff. The paleo sea cliff is now preserved as the

riser separating floodplain from Nooksack River delta deposits (Figure 15d).

5.7. Coastal Site With Negligible Late Holocene Relative Sea Level Change

[80] The stratigraphy at Chuckanut Cove (site CC, Figure 6) is consistent with stratigraphic observations at tectonically stable sites. At Chuckanut Cove, stratigraphy in cores consists of lithified glaciomarine drift overlain by a paleosol, in turn overlain by peat. The basal peat contact is at or below high tide level.

[81] We infer the Chuckanut Cove site records late Holocene submergence because glaciomarine drift and an overlying paleosol, which were formerly above sea level, are now submerged. Therefore the site hosts gradual relative sea level rise in the late Holocene, a coastal response at sites without late Holocene tectonic uplift or subsidence [Beale, 1990].

6. Discussion

6.1. Active Faults

[82] We infer the existence of two previously unrecognized, active upper-plate faults, the Birch Bay and Sandy Point faults (Figure 16). We also infer a third candidate fault, the Drayton Harbor fault. Each of these faults has a trace length that extends from offshore to onshore based on aeromagnetic data (Table 4). The Birch Bay and Sandy Point faults offset Holocene landforms and/or deposits and both faults can be extended laterally along strike by association of magnetic contacts with sites of Holocene deformation. With the recognition of these Holocene faults, the actively deforming Cascadia forearc is now interpreted to extend at least 60 km north of the previously recognized northern limit. This revision of the northern bound of forearc deformation based on paleoseismology is consistent with the distribution of active forearc seismicity, which extends north of the U.S.-Canadian border [Hyndman et al., 2003].

[83] We use airborne, ground, and marine magnetic data to support primary paleoseismic evidence for Holocene deformation at Birch Bay, Sandy Point, and possibly Drayton Harbor. Figure 5 shows numerous other aeromagnetic lineaments. Low-amplitude magnetic lineaments in Pleistocene glacial terrain can be caused by a variety of geologic processes, and we do not believe all of the magnetic lineaments on Figure 5 are caused by faults and folds. However, the strong association between specific magnetic lineaments and independent geologic evidence at Birch Bay, Sandy Point, and Drayton Harbor is evidence that these three anomalies are caused by Holocene faults. Given the association of these specific magnetic contacts and mapped Holocene faults, we have a sound basis to extend Holocene fault traces away from paleoseismic sites using the associated magnetic contacts.

[84] We infer the Sandy Point fault has generated three coseismic uplift events since deceleration of rise in relative sea level about 6 ka. Total Holocene coseismic uplift is about 4 m. The last coseismic uplift was several centuries after 2060–2320 yr BP. The Sandy Point fault has a 12-km trace length as inferred from the linear extent of the Sandy Point magnetic contact.
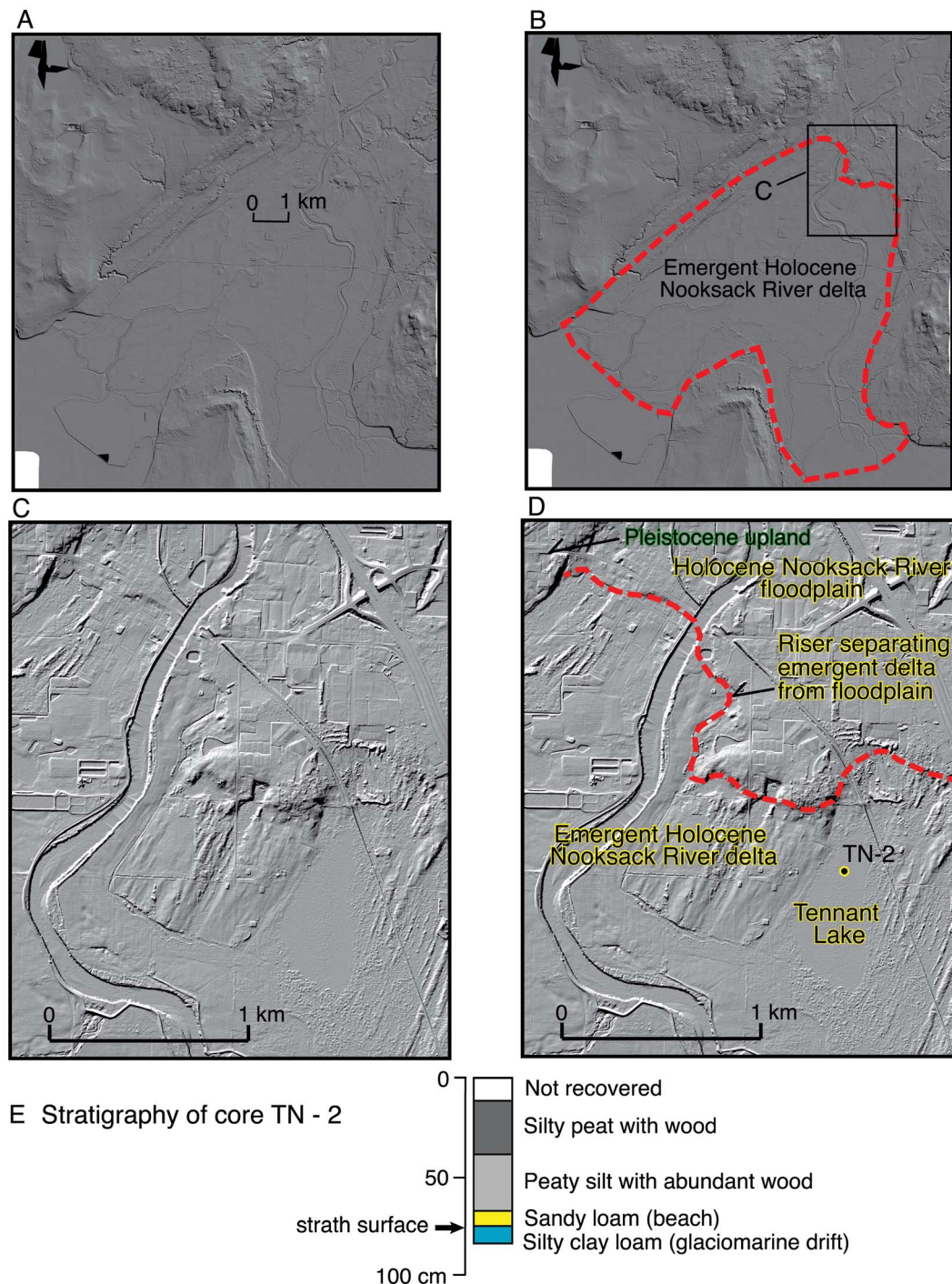
Figure 15. (a, b) LiDAR image showing the extent of the emergent late Holocene delta of the Nooksack River. (c, d) LiDAR image of Tennant Lake area 1.5 km south of Ferndale, Washington. LiDAR elevation data show a ca. 2 m-high scarp (red dashed line) that may define the backedge of a raised Holocene shoreline. South of the inferred shoreline is the emergent delta of the Nooksack River. North of the inferred shoreline is Holocene floodplain sediment deposited by the Nooksack River. Location of Figures 15 images depicted in Figure 6.

[85] We infer the Birch Bay fault was last active 1280–1070 yr BP, or shortly thereafter, at which time an earthquake displaced the ground surface at least 0.5 m and perhaps as much as 2 m up to the north. The Birch Bay fault is located on the coast at the juncture of simultaneously coseismically subsided and uplifted fault blocks (Figure 9). This coastal location correlates to a magnetic contact from which we infer a minimum fault trace length of 5 km from paleoseismic work and a maximum fault trace length of 24 km, which includes the associated magnetic contact length.
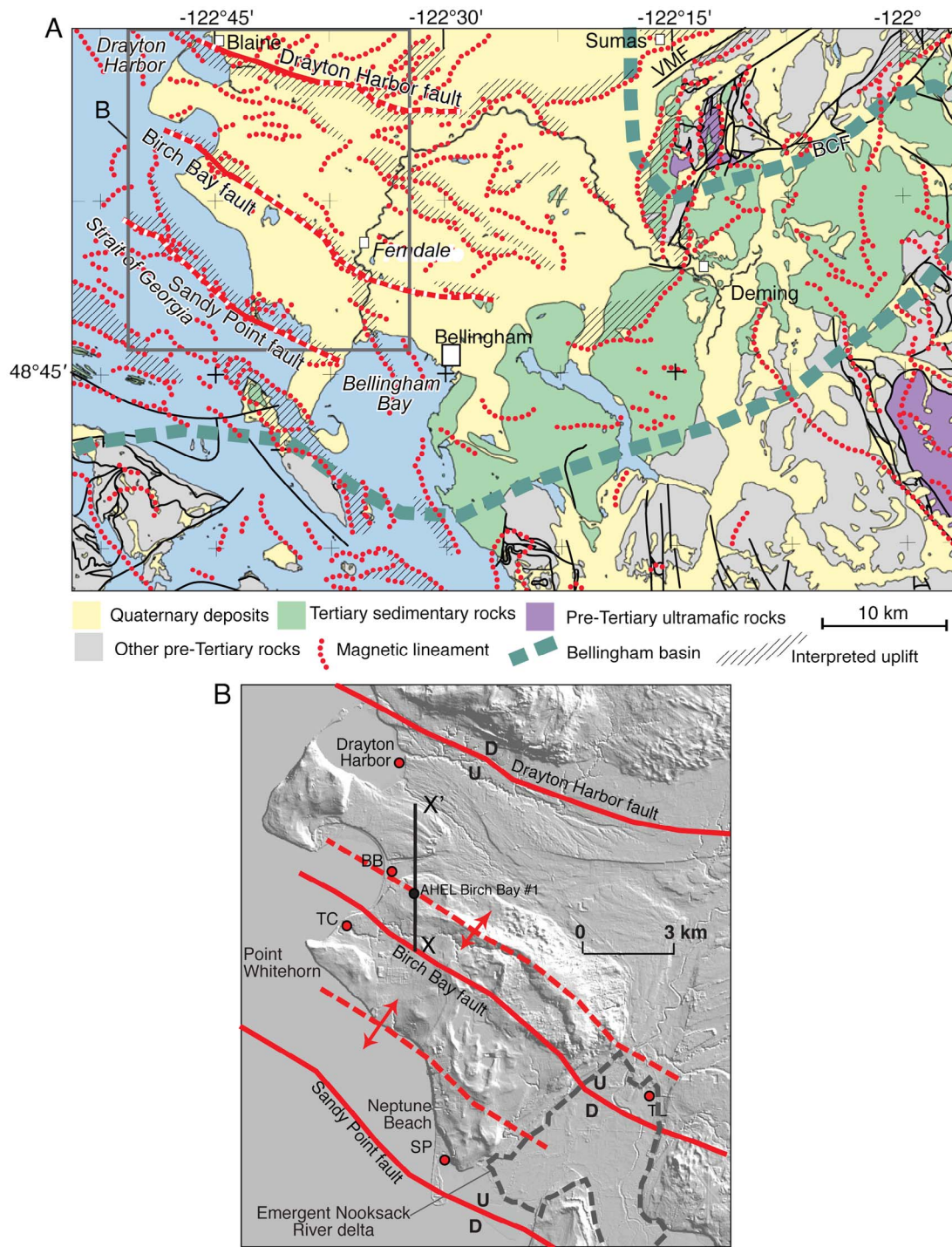
Figure 16. (a) Three Holocene faults (solid, bold red lines), which are identified from paleoseismic and LiDAR data, have been extended both onshore and offshore based on interpretations of gravity and magnetic anomalies. These extensions of Holocene faults are delineated by red-and-white dashed lines. Red dotted lines are interpreted magnetic contacts and black stipple indicates positive side of magnetic lineament; i.e., the uplifted side of a fault, assuming normal polarity strata. Geologic map from *Dragovich et al.* [2002]. Broad dashed line is margin of Bellingham basin, as shown in Figures 1 and 5. VMF, Vedder Mountain fault; BCF, Boulder Creek fault. (b) LiDAR image (acquired summer 2006 by U.S. Geological Survey) showing five paleoseismic study sites (red dots with block perimeters) and three Holocene faults (solid red lines) inferred from investigations described in text. Red dashed lines, anticline axes of folds in the hanging wall of the Sandy Point fault and the Birch Bay fault. Also shown is the track line of the seismic reflection profile reproduced in Figure 1d (X-X′). BB, Birch Bay; TC, Terrell Creek; SP, Sandy Point; TL, Tennant Lake.

Table 4. Attributes of Holocene Faults in Bellingham Basin

Fault Name	Trend	Trace Length[a] (km)	Maximum Limiting Age for Most Recent Earthquake[b] (yr BP)	Vertical Displacement in Most Recent Earthquake[c] (m)
Drayton Harbor fault	N60W	25 (8)	nd[d]	nd[d]
Sandy Point fault	N50W	12 (5)	2320[e]	1 m
Birch Bay fault	N54W	24 (6)	1280[f]	0.5–2 m[g]

[a]Determined from length of aero-, ground-, and boat-magnetic contacts correlated to mapped on-land fault trace lengths. Numbers in parentheses are trace lengths if one considers only the trace length that is inferred by either ground surface displacement (scarps) or ground displacement determined from paleo-environmental reconstructions using diatoms.

[b]Years before CE 1950; derived from radiocarbon age determinations, see Table 3 and discussion in text.

[c]Determined from paleoseismic investigations, see discussion in text.

[d]nd, not determined.

[e]2320 yr BP is the maximum limiting age for the next-to-youngest earthquake at Sandy Point; it is likely the youngest earthquake at Sandy Point is centuries younger than 2320 yr BP.

[f]1280 yr BP is the maximum limiting age for the time of sudden emergence of Birch Bay tidelands during the most recent earthquake, based on a 1280–1070 age on delicate wood detritus sampled at the base of black to dark brown peat (see Figure 11).

[g]The surveyed profiles support the inference from diatom observations that the vertical displacement associated with the fault slip that displaced Birch Bay relative to Terrell Creek was at least 0.5 m and may have been as much as 2 m. See text.

[86] Topographic data in conjunction with magnetic data pose the possibility of a Holocene Drayton Harbor fault. The discontinuous scarp on LiDAR imagery may offset Holocene (post-glacial) fluvial deposits. A ground magnetic traverse, surveyed across the Drayton Harbor scarp at a site where the scarp is topographically well defined, clearly depicts a shallow magnetic contact with up-thrown side consistent with the sense of vertical displacement inferred from the scarp-facing direction. But a magnetic contact does not confirm that a scarp is a Holocene fault scarp. Trench excavation across the scarp is needed to show Holocene faulting. Total length of the candidate Drayton Harbor fault trace, based on both the discontinuous LiDAR scarp and associated the magnetic contact (Figures 5 and 8), is 25 km (Table 4).

[87] The ratio of strike-slip to vertical displacement during earthquakes on the Birch Bay and Sandy Point faults is unknown, and the sense of dip slip (reverse or normal) is also not documented. The west-northwest trend of the faults and north-directed strain observed in GPS measurements [*McCaffrey et al.*, 2007] suggest that the faults are either dextral-oblique reverse faults or reverse faults. This interpretation assumes that modern strain reflects the long-term, ambient strain accumulation prior to the earthquakes.

[88] Support for the inference of reverse dip-slip motion on the Birch Bay fault comes from the anticline depicted in the seismic line in Figure 1d [*Hurst*, 1991]. The anticline axis is expressed in strata as young as Quaternary (Figure 1d), and the axis is 1.5–2.0 km north of the trace of the Birch Bay fault (Figures 9 and 16). We presume that this anticline strikes northwestward on the basis of its association with the Birch Bay magnetic anomaly, which has a northwest strike. The anticline therefore is in a position appropriate to be the hanging wall anticline of a Birch Bay reverse

fault, which strengthens the case that the Birch Bay fault accommodates reverse slip.

[89] The Sandy Point fault is also associated with a Quaternary-age anticline, and we suggest the anticline, which is 4–5 km north of the fault, developed in the hanging wall of the Quaternary- (and Holocene-) active Sandy Point fault (Figure 16b). The anticline is exposed in the coastal bluffs between Neptune Beach and Point Whitehorn (Figures 6 and 16b) where a Pleistocene stratified silt and clay, the 'Cherry Point silt' [*Easterbrook*, 1963], forms an open anticline with limb tilts of 7° south and 7° north. According to *Easterbrook* [1963], the silt was likely deposited horizontally and then tectonically tilted.

[90] Active fault deformation also may account for the observation that the late Holocene Nooksack delta is emergent. In the absence of tectonic influence on relative sea level, the Nooksack River delta should be gradually drowning because of late Holocene gradual relative sea level rise [*Beale*, 1990; *James et al.*, 2009]. To the contrary, the late Holocene delta of the Nooksack river is emergent (Figure 15b) and the Nooksack River's head of tide is of limited inland extent. The mechanism for late Holocene relative sea level fall, which has resulted in delta emergence, is unclear. However, one possible mechanism is coseismic slip, although not necessarily at the same time, on both the Sandy Point and Birch Bay faults. The delta laterally extends, southwest to northeast, across the hanging wall of the Sandy Point fault, the footwall of the Birch Bay fault and the hanging wall of the Birch Bay fault (Figure 16). Delta emergence may be the composite result of several instances of late Holocene coseismic uplift and folding of the two hanging walls in part compensated by relative subsidence of the intervening footwall.

[91] Despite site-specific data on timing of last earthquakes and magnitude of vertical displacement for the Sandy Point and Birch Bay faults, it is nonetheless difficult to further define fault slip geometry during earthquakes in this region. The landscape was reset in the late Pleistocene by the over-riding Cordilleran continental ice sheet, and such resetting precludes identification of fault-line scarps created by multiple earthquakes and thus largely precludes geomorphology-based mapping of fault trace lengths on land. And, in the case of the Birch Bay fault, the fault tip is blind and the most recent earthquake is expressed at the surface by a fold scarp that can only be indirectly located by the juxtaposition of footwall and hanging wall blocks (Figures 9 and 16).

[92] The Birch Bay fault nonetheless provides the best opportunity to constrain the magnitude of future earthquakes in the Bellingham basin. The trace length and range of permissible slip displacements involved in the last earthquake can be reasonably approximated based on both the paleo-environmental reconstructions of ground displacement and the pronounced aeromagnetic anomaly associated with the Holocene Birch Bay fault (Table 4). Based on an empirical approach that scales average slip displacement to moment magnitude [*Wells and Coppersmith*, 1994], and using a 0.5–2.0 m slip (Table 4), then the 1280–1070 year BP earthquake had a moment magnitude of about 6.0. Similarly, employing the same empirical approach but this time scaling trace length of reverse faults to moment magnitude [*Wells and Coppersmith*, 1994] and assuming the Birch Bay fault has an active trace length of 6 to 24 km, then the 1280–1070 year
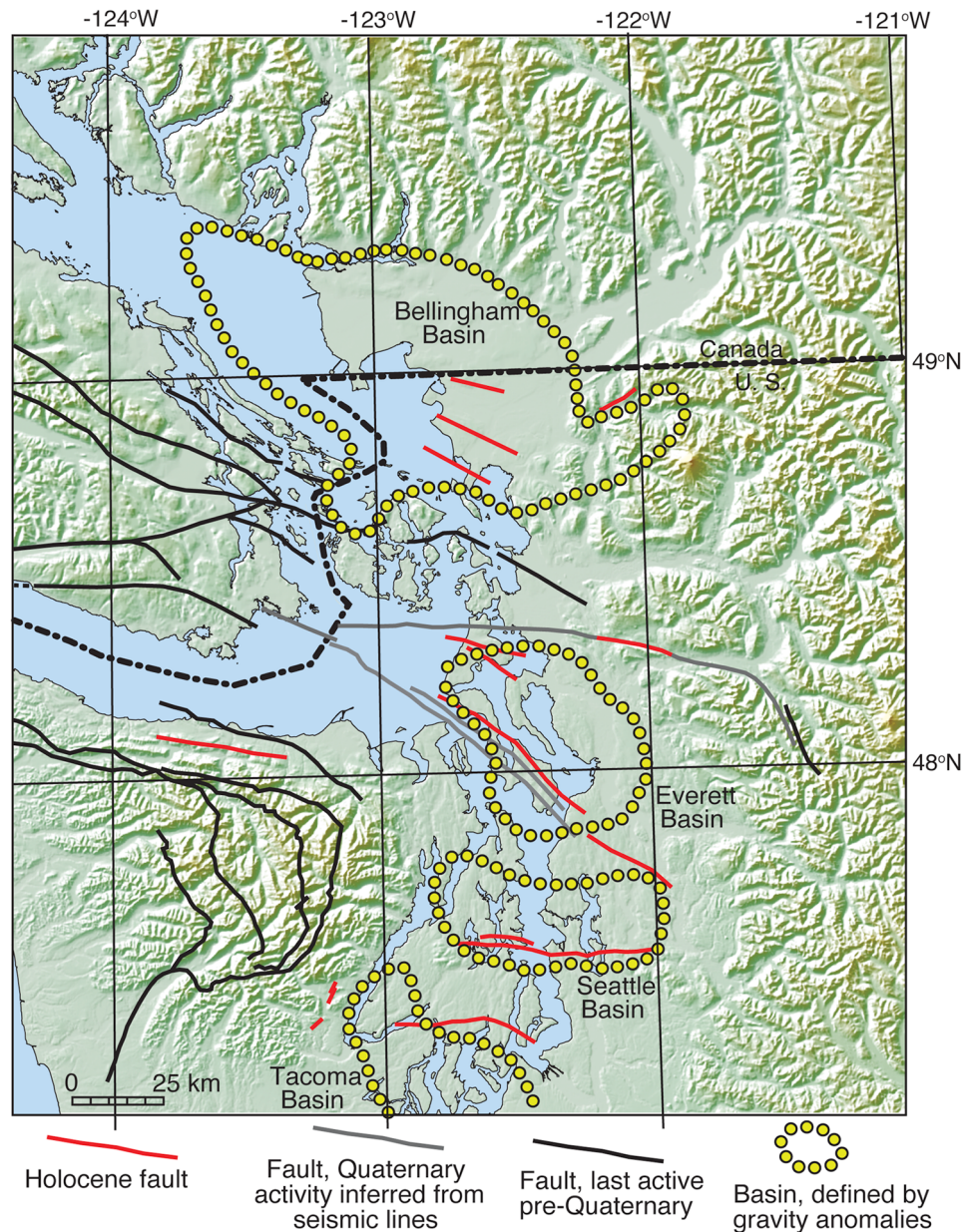
Figure 17. Puget-Fraser lowland of northwestern-most United States and southwestern British Columbia showing Holocene faults (red) and four northern Cascadia forearc basins that are identified based on gravity anomalies. The Holocene faults, which are concentrated in the lowlands, are shown in the context of other faults that either have inferred Quaternary activity based on seismic line interpretation (gray) or have no known Quaternary activity (black). Although some of the Holocene faults are basin-bounding or near the margins of basins, the faults as a whole do not clearly delineate the four major basins.

BP (Table 4) earthquake had a moment magnitude in the range of 6.0–6.5.

[93] Although such moment magnitude estimates are at best rough approximations, an earthquake with moment magnitude approaching or surpassing 6.0 could deform the seafloor and generate tsunami, especially given that the western part of the Birch Bay fault is offshore. The presence of a sand layer immediately above the buried soil in cores on the Terrell Creek lowland (Figure 6), which is adjacent to the offshore extent of the Birch Bay fault (Figure 16b), provides

support for the interpretation that the Birch Bay fault is tsunamigenic.

6.2. Bellingham Basin Lends Insight to Role of Holocene Faults in Evolution of Northern Cascadia Forearc Basins

[94] Although we identify the Bellingham Basin as the northernmost of a set of four forearc basins with Holocene deformation (Figure 17), the Bellingham Basin as a geologic structural basin dates back at least to the mid Tertiary and the basin has been recognized in the literature since the 1960s

[*Miller and Misch*, 1963]. Furthermore, the Bellingham Basin may be actively deforming in a manner dissimilar to its neighboring forearc basins. The Bellingham Basin is situated in the northernmost part of the forearc where Juan de Fuca-Pacific plate convergence is perpendicular to the margin, unlike oblique convergence to the south at the latitude of the Seattle and Everett basins (Figure 1a). The forearc at the latitude of Birch Bay north to the Canadian border may be responding to northeast-directed motion of the southern Vancouver Island block [*McCaffrey et al.*, 2007], as well as northward-directed motion of the northern Cascadia forearc. Therefore the Quaternary tectonics of the Bellingham Basin may be different from that of basins farther south in the forearc in that contemporary deformation is northeast to north-northeast directed contraction.

[95] In the Bellingham basin, the trends of active faults relative to the configuration of the basin margin do not have a systematic pattern, and the evolution of the Bellingham structural basin through faulting is unclear. For example, active faults associated with the Bellingham Basin do not lie along the margins of the basin. The Holocene-active Birch Bay and Sandy Point faults, as well as the candidate Holocene-active fault at Drayton Harbor, are located within the Bellingham Basin and not on or near the basin margin. Indeed, at the longitude of Sandy Point and Birch Bay, there are no recognized Holocene-active faults on the northern bound to the Bellingham Basin. Such faults, if extant, would be 15–20 km north of the international border.

[96] The other Holocene fault in the Bellingham basin, the Boulder Creek fault [*Barnett et al.*, 2006], is situated at the northeastern extent of the Bellingham Basin. Long-term displacement on the Boulder Creek fault has been up to the north, consistent with its position along the northeastern boundary of the Bellingham Basin (Figure 17). The active trace of the Boulder Creek fault, however, is up to the south [*Barnett et al.*, 2006], contrary to what would be expected of a simple basin-bounding fault. We speculate that the modern up-to-the-south displacement could reflect reactivation of the long-lived Boulder Creek fault as a backthrust.

[97] Holocene faults approximately define the width of the Puget lowland but are not always clearly associated with basin formation in the northern Cascadia forearc (Figure 17). At the one extreme, the Seattle fault is an example of a Cascadia forearc basin reverse fault that is clearly associated with a basin boundary. The Seattle fault defines the south end of the Seattle basin and the Seattle fault can account for uplift of the south edge of this basin [*Pratt et al.*, 1997; *Blakely et al.*, 2002]. At the other extreme, some Holocene-active faults do not overlie any of the four basins, and some basin margins are not bounded by Holocene active faults (Figure 17). The Boulder Creek fault is a basin-bounding fault that has a Holocene displacement sense opposite to what would be expected if the bounding fault was basin-generating. Still other Holocene-active faults are located in part along basin margins, such as the Tacoma fault and the Southern Whidbey Island fault, but only in the case of the Seattle fault does the seismically imaged fault both define the basin boundary and clearly account for the juxtaposition of uplifted block and adjacent Quaternary basin fill [*Pratt et al.*, 1997; *Blakely et al.*, 2002]. Given that only a subset of northern Cascadia forearc Holocene faults are situated on the

margins of structural basins, Holocene faults are only locally contributing to basin growth in Quaternary time.

7. Conclusion

[98] The emerging tectonic framework shows the northern Cascadia forearc as a north-south corridor accommodating northward contraction in part accommodated on Holocene faults. The deforming corridor hosts four structural basins defined by gravity anomalies, the Bellingham Basin being the northernmost of the four. Multiple data sets provide evidence that three west-northwest-trending active faults, Sandy Point, Birch Bay and Drayton Harbor faults, occur within the Bellingham basin at or a few kilometers south of the U. S.-Canadian border. The faults are 60 km north of the previously recognized northern limit of active faulting in the forearc. The faults are capable of producing earthquakes in the 6.0–6.5 moment magnitude range and may pose a seismic hazard to the lowland urban corridor between Vancouver, Canada and Bellingham, Washington. Although not recognized to date, it is possible that Holocene faults extend to the northern bound of the Bellingham Basin.

Appendix A

A1. Diatom Microscope Investigation of Water-Mounted Samples, Terrell Creek Core TC06-A

[99] Mud above peat-mud contact at 66 cm depth: Sample contained abundant marine organisms, including foraminifera. The marine diatoms observed include *Hyalodiscus sp.*, *Melosira moniliformis*, *Thallassiosira cf. decepiens*, and *Arachnodiscus ehrenbergii*. *Arachnodiscus ehrenbergii* (= *A. japonicus*) is a littoral species, most commonly found in beach environments. Several cosmopolitan brackish-freshwater taxa were observed. Interpretation: tidal flat assemblage, based on the marine diatom taxa and foraminifera.

[100] Soil below peat-mud contact at 66 cm depth: Sample contained a low concentration of diatoms, and those present were mostly broken valves, which are typical of soil diatom assemblages. The most common diatoms were *Diploneis cf. stromeii / D. cf. interrupta* and *Pinnularia sp.* Interpretation: soil diatom flora in a freshwater to brackish water setting.

A2. Diatom Microscope Investigation of Water-Mounted Samples, Sandy Point Soil Pit SP06B

[101] 12 cm depth: *Pinnularia* and *Eunotia* fragments dominate the assemblage. Interpretation: wet soil environment, freshwater wetland.

[102] 28 cm depth: *Pinnularia sp.*, *Gomphonema sp.*, *Navicula cf. delawarensis*, and *Eunotia sp.* dominate the assemblage. Interpretation: freshwater marsh diatom flora.

[103] 39 cm depth: *Gomphonema sp.* (*G. cf. gracile* or *G. cf. subclavatum*) dominates the assemblage, followed by *Pinnularia cf. viridis, Eunotia sp.*, other *Pinnularia sp.* fragments, and *Cosmioneis pusilla.*

[104] 40 cm depth: Abrupt contact between paleo-freshwater wetland above and paleo-tide flat below.

[105] 45 cm depth: Sample had abundant diatoms. *Gomphonema cf. gracile/subclavatum* and *Pinnularia sp.* fragments dominated the assemblage. Other diatoms of note include: *Arachnodiscus ehrenbergii, Hantzschia amphioxis,*

Eunotia sp, Nitzschia sp., and *Navicula pusilla.* Interpretation: brackish-marine diatom flora.

[106] 50 cm depth: Sample flora compositionally similar to the sample from 45 cm depth but contained about 10 times the amount of *Arachnodiscus ehrenbergii* (mostly as fragments). Interpretation: nearshore marine flora, tide flat or low energy beach environment.

A3. Mounting Technique for Birch Bay Diatom Analysis

[107] We prepared sediments for diatom analysis with an initial treatment of hot 30% hydrogen peroxide and removed fine mineral particles with differential settling during multiple distilled water rinses. We made permanent microscope slides by settling and drying a diluted aliquot of the diatom-rich sediment onto square 22-mm coverslips and inverting the coverslips on clean glass slides using Naphrax as a mounting medium (n = 1.65).

References

Barnett, E. A., H. M. Kelsey, B. L. Sherrod, R. J. Blakely, J. F. Hughes, E. R. Schermer, R. A. Haugerud, C. S. Weaver, and E. Siedlecki (2006), Active faulting at the northeast margin of the greater Puget lowland: A paleoseismic and magnetic-anomaly study of the Kendall scarp, Whatcom County, Northwest Washington, *Eos Trans. AGU*, *87*(52), Fall Meet. Suppl., Abstract S31A-0183.

Beale, H. (1990), Relative rise in sea-level during the late Holocene at six salt marshes in the Puget basin, Washington, MSc thesis, Dep. of Geol., West. Wash. Univ., Bellingham.

Berryman, K. R. (1993), Age height and deformation of Holocene marine terraces at Mahia Peninsula, Hikurangi subduction margin, New Zealand, *Tectonics*, *12*, 1347–1364, doi:10.1029/93TC01542.

Birks, H. J. B. (1995), Quantitative palaeoenvironmental reconstructions, in *Statistical Modeling of Quaternary Science Data, Technical Guide No. 5*, edited by D. Maddy and J. S. Brew, pp. 161–254, Quat. Res. Assoc., London.

Blakely, R. J. (1995), *Potential Theory in Gravity and Magnetic Applications*, Cambridge Univ. Press, New York, doi:10.1017/CBO9780511549816

Blakely, R. J., R. E. Wells, and C. S. Weaver (1999), Puget Sound aeromagnetic maps and data, *U.S. Geol. Surv. Open File Rep.*, *99-514*.

Blakely, R. J., R. E. Wells, C. S. Weaver, and S. Y. Johnson (2002), Location, structure, and seismicity of the Seattle fault zone, Washington: Evidence from aeromagnetic anomalies, geologic mapping, and seismic-reflection data, *Geol. Soc. Am. Bull.*, *114*, 169–177, doi:10.1130/0016-7606(2002)114<0169:LSASOT>2.0.CO;2.

Blakely, R. J., B. L. Sherrod, J. F. Hughes, M. L. Anderson, R. E. Wells, and C. S. Weaver (2009), Saddle Mountain fault deformation zone, Olympic Peninsula, Washington: Western boundary of the Seattle uplift, *Geosphere*, *5*, 105–125, doi:10.1130/GES00196.1.

Brocher, T. M., T. Parsons, R. J. Blakely, N. I. Christensen, M. A. Fisher, R. E. Wells, and the SHIPS Working Group (2001), Upper crustal structure in Puget lowland, Washington: Results from 1998 seismic hazards investigation in Puget Sound, *J. Geophys. Res.*, *106*, 13,541–13,564, doi:10.1029/2001JB000154.

Brocher, T. M., R. J. Blakely, and R. E. Wells (2004), Reinterpretation of the Seattle uplift, Washington, as a passive roof duplex, *Bull. Seismol. Soc. Am.*, *94*, 1379–1401, doi:10.1785/012003190.

Bucknam, R. C., E. Hemphill-Haley, and E. B. Leopold (1992), Abrupt uplift within the past 1700 years at southern Puget Sound, Washington, *Science*, *258*, 1611–1614, doi:10.1126/science.258.5088.1611.

Cashman, S. M., H. M. Kelsey, C. H. Erdman, H. Cutten, and K. B. Berryman (1992), Structural transect and analysis of strain partitioning across the forearc of the Hikurangi subduction zone, Hawke's Bay, North Island, New Zealand, *Tectonics*, *11*, 242–257, doi:10.1029/91TC02363.

Cisternas, M., et al. (2005), Predecessors to the giant 1960 Chile earthquake, *Nature*, *437*, 404–407, doi:10.1038/nature03943.

Clague, J. J., and T. S. James (2002), History and isostatic effects of the last ice sheet in southern British Columbia, *Quat. Sci. Rev.*, *21*, 71–87, doi:10.1016/S0277-3791(01)00070-1.

Dragovich, J. D., D. K. Norman, R. A. Haugerud, and P. T. Pringle (1997), Geologic map and interpreted geologic history of the Kendall and Deming 7.5-minute quadrangles, Western Whatcom County, Washington, *Open File Rep. 97–2*, Wash. Div. of Geol. and Earth Res., Olympia.

Dragovich, J. D., R. L. Logan, H. W. Schasse, T. J. Walsh, W. S. Lingley Jr., D. K. Norman, W. J. Gerstel, T. J. Lapen, J. E. Schuster, and K. D. Meyers (2002), Geologic map of Washington: Northwest quadrant, *Geol. Map GM-50*, Wash. Div. of Geol. and Earth Res., Olympia.

Easterbrook, D. J. (1963), Late Pleistocene glacial events and relative sea level changes in the northern Puget lowland, *Geol. Soc. Am. Bull.*, *74*, 1465–1484, doi:10.1130/0016-7606(1963)74[1465:LPGEAR]2.0.CO;2.

Easterbrook, D. J. (1976), Geologic map of western Whatcom County, Washington, *U.S. Geol. Surv. Misc. Invest. Map*, *I-854-B*, scale 1:62,500.

Fulmer, C. V. (1975), Stratigraphy and paleontology of the type Blakeley and Blakely Harbor Formations, paper presented at Annual Convention of the Society of Economic Paleontologists and Mineralogists, Long Beach, Calif.

Gallup, W. B. (1957), Will these sedimentary basins [Pacific Coast] prove oil bearing?, *Oil Gas J.*, *55*, 142.

Haugerud, R. A., B. L. Sherrod, R. E. Wells, and T. Hyatt (2005), Holocene displacement on the Boulder Creek fault near Bellingham, Washington and implications for kinematics of deformation of the Cascadia forearc, *Geol. Soc. Am. Abstr. Programs*, *37*(7), 476.

Hemphill-Haley, E. (1995), Diatom evidence for earthquake-induced subsidence and tsunami 300 yr ago in coastal Washington, *Geol. Soc. Am. Bull.*, *107*, 367–378, doi:10.1130/0016-7606(1995)107<0367:DEFEIS>2.3.CO;2.

Hopkins, W. S. (1968), Subsurface Miocene rocks, British Columbia-Washington, a palynological investigation, *Geol. Soc. Am. Bull.*, *79*, 763–768, doi:10.1130/0016-7606(1968)79[763:SMRBCA]2.0.CO;2.

Hull, A. G. (1990), Tectonics of the 1931 Hawke's Bay earthquake, *N.Z. J. Geol. Geophys.*, *33*, 309–320, doi:10.1080/00288306.1990.10425689.

Hurst, P. D. (1991), Petroleum geology of the Bellingham basin, Washington, and evaluation of the AHEL and Partners Birch Bay No. 1 well, *Wash. Geol.*, *19*, 16–18.

Hyndman, R. D., S. Mazzotti, D. Weichert, and G. C. Rogers (2003), Frequency of large crustal earthquakes in Puget Sound-Southern Georgia Strait predicted from geodetic and geological deformation rates, *J. Geophys. Res.*, *108*(B1), 2033, doi:10.1029/2001JB001710.

James, T., E. J. Gowan, I. Hutchinson, J. J. Clague, J. V. Barrie, and K. W. Conway (2009), Sea-level change and paleogeographic reconstructions, southern Vancouver Island, British Columbia, Canada, *Quat. Sci. Rev.*, *28*, 1200–1216, doi:10.1029/j.quascirev.2008.12.022.

Johnson, S. Y. (1982), Stratigraphy, sedimentology, and tectonic setting of the Eocene Chuckanut Formation, northwest Washington, PhD thesis, 221 pp., Univ. of Wash., Seattle.

Johnson, S. Y., C. J. Potter, and J. M. Armentrout (1994), Origin and evolution of the Seattle Fault and Seattle Basin, Washington, *Geology*, *22*, 71–74, doi:10.1130/0091-7613(1994)022<0071:OAEOTS>2.3.CO;2.

Johnson, S. Y., C. J. Potter, J. M. Armentrout, J. J. Miller, C. A. Finn, and C. S. Weaver (1996), The southern Whidbey Island Fault: An active structure in the Puget lowland, Washington, *Geol. Soc. Am. Bull.*, *108*, 334–354, doi:10.1130/0016-7606(1996)108<0334:TSWIFA>2.3.CO;2.

Johnson, S. Y., S. V. Dadisman, J. R. Childs, and W. D. Stanley (1999), Active tectonics of the Seattle fault and central Puget Sound, Washington: Implications for seismic hazards, *Geol. Soc. Am. Bull.*, *111*, 1042–1053, doi:10.1130/0016-7606(1999)111<1042:ATOTSF>2.3.CO;2.

Johnson, S. Y., S. V. Dadisman, D. C. Mosher, R. J. Blakely, and J. R. Childs (2001), Active tectonics of the Devils Mountain fault and related structures, northern Puget lowland and eastern Strait of Juan de Fuca Region, Pacific Northwest, *U.S. Geol. Surv. Prof. Pap.*, *1643*, 45 p.

Johnson, S. Y., A. R. Nelson, S. F. Personius, R. E. Wells, H. M. Kelsey, B. L. Sherrod, R. Koehler, R. C. Witter, L. A. Bradley, and D. A. Harding (2004a), Evidence for late Holocene earthquakes on the Utsalady Point Fault, northern Puget lowland, Washington, *Bull. Seismol. Soc. Am.*, *94*(6), 2299–2316, doi:10.1785/0120040050.

Johnson, S. Y., R. J. Blakely, W. J. Stephenson, S. V. Dadisman, and M. A. Fisher (2004b), Active shortening of the Cascadia forearc and implications for seismic hazards of the Puget lowland, *Tectonics*, *23*, TC1011, doi:10.1029/2003TC001507.

Juggins, S. (2003), *C2 User Guide and Software for Ecological and Palaeoecological Data Analysis and Visualization*, 69 pp., Univ. of Newcastle, Newcastle upon Tyne, U. K.

Kanamori, H. (1995), The Kobe (Hyogo-ken Nanbu), Japan, earthquake of January 16, 1995, *Seismol. Res. Lett.*, *66*, 6–10, doi:10.1785/gssrl.66.2.6.

Kelsey, H. M., S. M. Cashman, K. R. Berryman, and S. Beanland (1995), Structural evolution along the inner forearc of the obliquely convergent Hikurangi margin, New Zealand, *Tectonics*, *14*, 1–18, doi:10.1029/94TC01506.

Kelsey, H. M., A. Hull, S. Cashman, K. Berryman, P. Cashman, J. Trexler, and J. Begg (1998), Paleoseismology of an active reverse fault in a fore-arc setting: The Poukawa fault zone, Hikurangi forearc, New Zealand, *Geol. Soc. Am. Bull.*, *110*, 1123–1148, doi:10.1130/0016-7606(1998) 110<1123:POAARF>2.3.CO;2.

Kelsey, H. M., B. L. Sherrod, S. Y. Johnson, and S. V. Dadisman (2004), Land-level changes from a late Holocene earthquake in the northern Puget lowland, Washington, *Geology*, *32*, 469–472, doi:10.1130/G20361.1.

Kelsey, H. M., B. L. Sherrod, A. R. Nelson, and T. M. Brocher (2008), Earthquakes generated from bedding-plane-parallel reverse faults above an active wedge thrust, *Geol. Soc. Am. Bull.*, *120*, 1581–1597, doi:10.1130/B26282.1.

Kovanen, D. J., and D. J. Easterbrook (2002), Timing and extent of Allerod and Younger Dryas age (ca. 12,500–10,000 ^{14}C yr BP) oscillations of the Cordilleran ice sheet in the Fraser Lowland, western North America, *Quat. Res.*, *57*, 208–224, doi:10.1006/qres.2001.2307.

Kovanen, D. J., and O. Slaymaker (2003), Lake Terrell upland glacial resurgences and implications for late-glacial history, northwestern Washington state, U.S.A., *Can. J. Earth Sci.*, *40*, 1767–1772, doi:10.1139/e03-074.

Little, T. A., R. Van Dissen, E. Schermer, and R. Carne (2009), Late Holocene surface ruptures on the southern Wairarapa fault, New Zealand: Link between earthquakes and the uplifting of beach ridges on a rocky coast, *Lithosphere*, *1*, 4–28, doi:10.1130/L7.1.

Mazzotti, S., H. Dragert, R. Hyndman, M. M. Miller, and J. Henton (2002), GPS deformation in a region of high crustal seismicity: N. Cascadia fore-arc, *Earth Planet. Sci. Lett.*, *198*, 41–48, doi:10.1016/S0012-821X(02)00520-4.

Mazzotti, S., H. Dragert, J. Henton, M. Schmidt, R. Hyndman, T. Jams, Y. Lu, and M. Craymer (2003), Current tectonics of northern Cascadia from a decade of GPS measurements, *J. Geophys. Res.*, *108*(B12), 2554, doi:10.1029/2003JB002653.

McCaffrey, R., M. D. Long, C. Goldfinger, P. C. Zwick, J. L. Nabelek, C. K. Johnson, and C. Smith (2000), Rotation and plate locking at the southern Cascadia subduction zone, *Geophys. Res. Lett.*, *27*, 3117–3120, doi:10.1029/2000GL011768.

McCaffrey, R., A. I. Qamar, R. W. King, R. Wells, G. Khazaradze, C. A. Williams, C. W. Stevens, J. J. Vollick, and P. C. Zwick (2007), Fault locking, block rotation and crustal deformation in the Pacific Northwest, *Geophys. J. Int.*, *169*(3), 1315–1340, doi:10.1111/j.1365-246X.2007.03371.x.

Miller, G. D., and P. Misch (1963), Early Eocene angular unconformity at western front of the Northern Cascades, Whatcom County, Washington, *Am. Assoc. Pet. Geol. Bull.*, *47*, 163–174.

Nelson, A. R., S. Y. Johnson, H. M. Kelsey, R. E. Wells, B. L. Sherrod, S. K. Pezzopane, L. Bradley, R. D. Koehler, and R. C. Bucknam (2003), Late Holocene earthquakes on the Toe Jam Hill fault, Seattle fault zone, Bainbridge Island, Washington, *Geol. Soc. Am. Bull.*, *115*, 1388–1403, doi:10.1130/B25262.1.

Phillips, J. D., R. O. Hansen, and R. J. Blakely (2007), The use of curvature in potential-field interpretation, *Explor. Geophys.*, *38*, 111–119, doi:10.1071/EG07014.

Pollitz, F. F., and I. S. Sacks (1997), The 1995 Kobe, Japan, earthquake: A long-delayed aftershock of the offshore 1944 Tonankai and 1946 Nankaido earthquakes, *Bull. Seismol. Soc. Am.*, *87*, 1–10.

Pratt, T. L., S. Johnson, C. Potter, W. Stephenson, and C. Finn (1997), Seismic reflection images beneath Puget Sound, western Washington State: The Puget lowland thrust sheet hypothesis, *J. Geophys. Res.*, *102*, 27,469–27,489, doi:10.1029/97JB01830.

Reimer, P. J., et al. (2004), IntCal04 terrestrial radiocarbon age calibration, 0–26 cal kyr BP, *Radiocarbon*, *46*, 1029–1058.

Sherrod, B. L. (2001), Evidence for earthquake induced subsidence about 1100 yr ago in coastal marshes of southern Puget Sound, Washington, *Geol. Soc. Am. Bull.*, *113*, 1299–1311, doi:10.1130/0016-7606(2001) 113<1299:EFEISA>2.0.CO;2.

Sherrod, B. L., R. C. Bucknam, and E. B. Leopold (2000), Holocene relative sea-level changes along the Seattle Fault at Restoration Point, Washington, *Quat. Res.*, *54*, 384–393, doi:10.1006/qres.2000.2180.

Sherrod, B. L., T. M. Brocher, C. S. Weaver, R. C. Bucknam, R. J. Blakely, H. M. Kelsey, A. R. Nelson, and R. Haugerud (2004), Holocene fault scarps near Tacoma, Washington, USA, *Geology*, *32*, 9–12, doi:10.1130/G19914.1.

Sherrod, B. L., R. J. Blakely, C. Weaver, H. M. Kelsey, E. Barnett, and R. Wells (2005), Holocene fault scarps and shallow magnetic anomalies along the southern Whidbey Island fault zone near Woodinville, Washington, *U.S. Geol. Surv. Open File Rep.*, *2005-1136*, 35 p.

Sherrod, B. L., R. J. Blakely, C. S. Weaver, H. M. Kelsey, E. Barnett, L. Liberty, K. L. Meagher, and K. Pape (2008), Finding concealed active faults: Extending the southern Whidbey Island fault across the Puget lowland, Washington, 2008, *J. Geophys. Res.*, *113*, B05313, doi:10.1029/2007JB005060.

Simpson, R. W., R. C. Jachens, R. J. Blakely, and R. W. Saltus (1986), A new isostatic residual gravity map of the conterminous United States with a discussion of the significance of isostatic residual anomalies, *J. Geophys. Res.*, *91*, 8348–8372, doi:10.1029/JB091iB08p08348.

Wells, D. L., and K. J. Coppersmith (1994), New empirical relationships among magnitude, rupture length, rupture width, rupture area and surface displacement, *Bull. Seismol. Soc. Am.*, *84*, 974–1002.

Wells, R. E., C. S. Weaver, and R. J. Blakely (1998), Forearc migration in Cascadia and its neotectonic significance, *Geology*, *26*, 759–762, doi:10.1130/0091-7613(1998)026<0759:FAMICA>2.3.CO;2.

Witter, R. C., H. M. Kelsey, and E. Hemphill-Haley (2003), Great earthquakes and tsunamis of the past 6700 years, Coquille River estuary, southern coastal Oregon, *Geol. Soc. Am. Bull.*, *115*, 1289–1306, doi:10.1130/B25189.1.

Zong, Y., and B. Horton (1999), Diatom-based tidal-level transfer functions as an aid in reconstructing Quaternary history of sea-level movements in the UK, *J. Quat. Sci.*, *14*(2), 153–167, doi:10.1002/(SICI)1099-1417 (199903)14:2<153::AID-JQS425>3.0.CO;2-6.

Zong, Y., I. Shennan, R. Combellick, S. Hamilton, and M. Rutherford (2003), Microfossil evidence for land movements associated with the AD 1964 Alaska earthquake, *Holocene*, *13*(1), 7–20, doi:10.1191/0959683603hl590rp.

R. J. Blakely, U.S. Geological Survey, 345 Middlefield Rd., Menlo Park, CA 94025, USA. (blakely@usgs.gov)

R. A. Haugerud and B. L. Sherrod, U.S. Geological Survey, University of Washington, Box 351310, Seattle, WA 98195, USA. (haugerud@u.washington.edu; bsherrod@usgs.gov)

H. M. Kelsey, Department of Geology, Humboldt State University, Arcata, CA 95521, USA. (hmk1@humboldt.edu)